Turbulence Kinetic Energy Budget and Conditional Sampling of Momentum, Scalar, and Intermittency Fluxes in Thermally Stratified Wind Farms

Naseem Ali [1], Nicholas Hamilton [2], Marc Calaf [3], and Raúl Bayoán Cal [1]
[1] *Department of Mechanical and Materials Engineering, Portland State University, Portland, Oregon, USA*
[2] *National Renewable Energy Laboratory, Golden, Colorado, USA, and*
[3] *Department of Mechanical Engineering, University of Utah, Salt Lake City, Utah, USA*
(Dated: December 20, 2018)

A description of the turbulence kinetic energy budget is investigated to understand the dynamics and turbulence energy transfer between the atmospheric boundary layer and large wind farms. The turbulence kinetic energy budget terms are a dominant factor in explaining the energy supply process in wind farms. Large eddy simulations are used to generate the thermally stratified wind turbine array boundary layer, where stable and unstable conditions are considered. The wakes represent a sink of mean kinetic energy and turbulence transport attempts to redistribute energy in the wake region. The energy balance between the budget terms is dependent on the physical location in the wind farm. During the unstable scenario, turbulence is driven by the production, transport, and buoyancy terms. Further, the contribution of the turbulence kinetic energy budget terms is reduced with increasing stability, especially above the shear layer, where the mechanical production is the dominant term. Pressure diffusion redistributes the turbulent energy from the streamwise direction into the other components of the normal Reynolds stresses. This distinctive feature of the changing thermal stratification is presented through studying the quadrant analysis. The momentum ejection and sweep frequencies are comparable and dominant. The scalar flux shows an increase in the contribution of the negative correlation in the quadrants. The quadrant analysis is extended to include the intermittency based on the pointwise Hölder exponents. The positive correlations are dominant in the wake and higher layer of the domain for both considered cases.

I. INTRODUCTION

The variable characteristics of the atmospheric boundary layer (ABL) flow are a consequence of the differential heating throughout a diurnal cycle, and are tightly related to the time varying production of turbulence, changing the corresponding contributions to the turbulent kinetic energy budget [1]. Installation of wind farms further increases the complexity and changes the structure of the flow [2–4]. The interaction of wind farms with the time-changing thermal stratification in the ABL can be highlighted through the evaluation of the mean and turbulent kinetic energy budget. As initially proposed by Cal et al. [5] and Calaf et al. [6], the power extracted by the wind turbine is of the same order of magnitude as the vertical flux of mean kinetic energy yet the production term is also a term of leading order within this balance. Consequently, considering the linkage between the mean kinetic energy and turbulence kinetic energy, the production term, $\overline{u_i'u_j'}\partial U_i/\partial x_j$, comes to the forefront as this term is responsible for, both, adding kinetic energy to the turbulence and in other hand subtracting energy from the mean flow. Note that the production term represents the dissipation in the mean kinetic energy. Therefore, if one was able to control this term based on the remaining terms of the turbulence kinetic energy budget, it would provide means to potentially boost wake recovery and overall energy harvesting. Viestenz and Cal [7] showed experimentally that the turbulent flux and the production term lead to power fluctuations of 30% of the mean power.

In the mean kinetic energy budget, the footprint of thermal stratification highlights the most important terms that deplete the energy, vertical flux in the unstable case and advection in the stable case [8]. Other events such as the power law, mixing decay, velocity reduction, and turbulence intensity are also related to thermal stratification effects [9–11]. It is therefore evident that a turbulence kinetic energy budget and transport of the Reynolds stress terms play major roles in the recovery process of mean kinetic energy in the wake of wind turbines as well as on the overall power harvested by a wind farm. Of particular interest is determining the influence of the relative contribution of different physical processes on the energy balance based on the thermal stratification. Within stable and unstable stratification conditions, the flow during the stable regime is driven by strong turbulent advection due to the bulk motion of the flow resultant from the low-level jet (LLJ), while during the unstable regime, turbulence is created and transported by large eddies driven via buoyancy forces [8]. Xie and Archer [12] used large eddy simulations to study the effect of the atmospheric thermal stratification of wind-turbine wake of the single and wind farm. Their results showed that the characteristic parameters of the wake of the single turbine, including the velocity deficit, thermal distribution and TKE, is highly correlated with stability. Thermal stratification changed the flow separation in the wind farm; less separation is found for the unstable case. With stability the TKE in the wind farm increases. The TKE is anti-correlated with the background turbulence of the atmospheric boundary layer. Ghaisas et al. [13] studied the effects of the stability (neutral, moderately unstable and stable) and wind farm configuration (turbines aligned versus staggered with respect to the wind) simultaneously. Their results highlighted that under unstable condition, the vertical mixing is enhanced and leads to faster recovery of velocity deficits, and that the lateral spread of wakes is significant. Abkar and Porté-Agel [14] investigated the influence of thermal stability on the wake of wind turbine. The spatial distribution of the mean velocity and wake meandering downstream of the turbine are highly correlated with the atmospheric stability. The growth rate of the wake under unstable scenario is about 2.4 times larger than that of the stable one. Here, the distinct terms conforming to the turbulence kinetic energy budget are considered in light of energy extraction.

To date, only limited studies have considered the effect of thermal stratification on the turbulent kinetic energy budget and the effect of the scalar flux on wind farms. Thus, less is known about the thermal stratification effects on conditional sampling in the very large wind farm and how the variations of ejection and sweep characteristics account for momentum and scalar fluxes. Therefore, it is of interest to: (1) Investigate the turbulence kinetic energy budget terms with respect to different thermal stratification regimes, (2) Quantify the second- and third-order correlations between the velocity and scalar (pressure and temperature) fields, and (3) Characterize the turbulent structures associated with momentum and scalar transport. The following work is organized as follows: Section II outlines the turbulence kinetic energy budget and conditional sampling; section III presents in detail large eddy simulations; section IV discusses the results; finally, section V outlines the main findings along with and future work.

II. THEORY

The general presentation of the TKE budget and conditional sampling for the momentum and scalar flux are reviewed in this section, these contain the correlations between the velocity and scalar quantities (pressure and temperature) and provide a basis to reveal the energy transfer mechanisms in thermally stratified wind plants.

A. Turbulence Kinetic Energy Budget

The turbulent kinetic energy (TKE) budget delineates the relative contributions of physical processes that govern the motion of the turbulent flow. Due to the multi-scale nature of wind turbine wake, the TKE budget terms (advection, production, buoyancy, etc.) contribute to the flow in a complex way. The presence of wind turbines in the ABL modifies the surface boundary layer in unique ways and impose further term to the TKE budget. Wind turbines introduce aerodynamic drag on the flow and generate turbulent motions seen as wakes, meaning that an additional source of TKE extracts kinetic energy from the mean flow. This additional term modifies the balance between competing elements of the TKE budget, changing the energy cascade by imposing new scales to the flow (wake scales). Abkar and Porté-Agel [15] studied the mean and turbulent kinetic energy budgets inside and above the neutrally stratified wind farms. Their results showed that the turbine-top level holds the peak of the shear production and dissipation rate, and their magnitude increase as the turbine spacing decreased. Chamorro et al. [16] provided a scale-by-scale energetic description of the wake behind a model wind turbine, and estimated the energy-containing scales through scaling the energy dissipation. They pointed out that turbine induces strong turbulent energy at a relatively high-frequency range, and that turbulent production is maximum at top-tip height, and the rotor area is marked with strong dissipation.

In the context of a vegetated canopy, Wilson [17] presented the TKE budget in a manner that splits the budget into two different scales, turbulent shear kinetic energy (SKE) and turbulent wake kinetic energy. This mathematical split assumes that the total TKE is conserved, assuming that a canopy acts a sink of kinetic energy for the large scales and a source for the small scales. Similarly, Leclerc et al. [18] used this approach and observed that the drag element of canopy is the primary sink term in the SKE budget, and shear production is the primary source in the upper canopy. Morse et al. [19] showed that the shear production term is counteracted by vertical advection and pressure redistribution. In this regards, different turbulence-resolving models, such as large eddy simulations (LES), are used to investigate the effect of the pressure in convective and neutral atmospheric boundary-layer flows [20–23].

Modeling the pressure-strain term is one of the major challenges in closure turbulence modeling for numerical climate applications and weather prediction models [22–24]. The effect of the shear and buoyancy in the flow is alleviated by the pressure term as it redistributes the kinetic energy between the velocity components, and reduces the turbulence anisotropy. Rotta [25] proposed the first pressure-strain model which has since been applied to simulate the entire pressure term. For example, Launder et al. [26] modeled slow turbulence-turbulence contribution with the pressure gradient-scalar covariance. Numerous more elaborate nonlinear models for the pressure terms also exist (e.g., Lumley [27]; Ristorcelli et al. [28]; Craft et al. [29]). In different cases, especially in flows with large departures from isotropy, nonlinear models performed better than linear models, such as boundary-layer flows affected by buoyancy and/or rotation. However, the nonlinear models mostly consist of complex expressions which are computationally expensive, especially in geophysical applications [21, 24]. Turbulence-resolving models are used to investigate and develop turbulence closure models and to determine the model constants. Experimentally, direct measurements of the pressure-strain are rather difficult especially in the atmospheric boundary layer given that the atmospheric pressure fluctuations are small relative to the mean pressure. In addition, pressure probes disturb the pressure field and distort measurements [30–32].

By nature, the TKE budget is directly related to the physical mechanisms that generate, transport, and destroy turbulence. The weight of each term identifies the flow stability and the ability of the flow to decay or produce turbulence [1]. The TKE budget equation for the resolved scales in the LES framework is given by Equation (1),

$$\frac{\partial \overline{e}}{\partial t} + \overline{\widetilde{u}}_j \frac{\partial \overline{e}}{\partial x_j} = +\delta_{i3} \frac{g}{\overline{\theta}} (\overline{u_i' \theta'}) - \overline{\tau}'_{ij} \frac{\partial \overline{\widetilde{u}}_i}{\partial x_j} - \frac{\partial (\overline{u_j' \overline{e}})}{\partial x_j} - \frac{1}{\overline{\rho}} \frac{\partial (\overline{u_i' p'})}{\partial x_i} - \frac{\partial \overline{\tau_{ij}' u_i'}}{\partial x_j} + \overline{f_i' u_i'} + \overline{\tau_{ij}' \widetilde{S}_{ij}}, \tag{1}$$

where $\overline{e} = 0.5\overline{u_i' u_i'}$ is the mean TKE for the resolved scales, i and j are indices taking values of 1, 2, and 3 for the three Cartesian coordinates (x, y, z), respectively, and (u, v, w) for the velocities. The prime ($'$) presents the fluctuating component, and tilde ($\tilde{}$) presents the instantaneous component. The p is the pressure, f is the force conveyed on the flow by the wind turbines, and $\overline{\tau}_{ij} = \overline{u_i' u_j'} + \overline{\tau}_{ij}^{sgs}$ represents the sum of the Reynolds stress and the sub-grid scale model (SGS) shear stress. The deviatoric part of the SGS stress is computed as $\tau_{ij}^{SGS} = -2\nu_t \widetilde{S}_{ij}$, where $\widetilde{S}_{ij}$ is the resolved strain rate tensor, $\widetilde{S}_{ij} = 0.5(\partial_j \widetilde{u}_i + \partial_i \widetilde{u}_j)$ and ν_t is the eddy viscosity for the SGS model. To simplify the subsequent comparison between the distinct atmospheric stability conditions and wind farm configuration, the different terms from the TKE budget equation are grouped as a transport term denoted by TR, a production term denoted by PR and a dissipation term denoted by ϵ_f. Consequently, the terms are defined as follows:

1. Transport term: $TR = TR_a + TR_t + TR_p + TR_{sgs}$, with

$$TR_a = -\overline{\widetilde{u}}_j \frac{\partial \overline{e}}{\partial x_j}, \;\; TR_t = -\frac{\partial (\overline{u_j' \overline{e}})}{\partial x_j}, \;\; TR_p = -\frac{1}{\overline{\rho}} \frac{\partial (\overline{u_i' p'})}{\partial x_i}, \;\; TR_{sgs} = -\frac{\partial \overline{\tau_{ij}' u_i'}}{\partial x_j}.$$

2. Production term: $PR = PR_b + PR_s + PR_{WT}$, with

$$PR_b = \delta_{i3} \frac{g}{\overline{\theta}} (\overline{u_i' \theta'}), \;\; PR_s = -\overline{\tau}_{ij}' \frac{\partial \overline{\widetilde{u}}_i}{\partial x_j}, \;\; PR_{WT} = +\langle \overline{f_i' u_i'} \rangle_{xy}, \tag{2}$$

3. Dissipation term:

$$\epsilon_f = \overline{\tau_{ij}' \widetilde{S}_{ij}}. \tag{3}$$

From left to right, the transport term is defined by the sum of the advection of TKE by the mean wind (TR_a), the turbulent transport of TKE which describes how TKE is moved around by turbulent eddies (TR_t), the pressure correlation term (TR_p), which describes how TKE is redistributed by pressure perturbations and TR_{sgs} which is the transport of the sub-grid scales. The production term includes buoyancy production denoted as PR_b, if the vertical flux is positive (during the day) or destruction if the vertical flux is negative (usually during the night), TKE production due to shear PR_s, and PR_{WT}, which is the turbulent production introduced in the flow by the wind turbines in terms of the wind turbines rate of work. Finally, ϵ_f denotes the dissipation of turbulence, which relates the transfer of energy from the resolved scales to the smaller scales, and is represented by the sub-grid scale model. Throughout, $\langle \cdot \rangle_{xy}$ represents a horizontal average operation over the entire domain in the $x-y$ spatial directions.

B. Quadrant Analysis

Identification of the coherent turbulent structures in high Reynolds number flows has been the subject of much theoretical and experimental research, being a vital topic in momentum, heat, and mass transport [33]. The distinctive patterns of the changing thermal stability are often analyzed by studying the flow coherence and through the covariance matrix. The thermal condition at the surface and turbulent mixing near the surface govern the dynamical stability of the atmospheric boundary layer. Different approaches have been used to investigate the structures of the atmospheric boundary layer and the wakes within wind farm flows such as proper orthogonal decomposition (POD) and conditional sampling [34–37].

POD provides the ability to describe and reconstruct coherent structures in the complex turbulent flow found in wind farms. The covariance matrix characterizes the correlation eigenvector and assesses the spatial distribution of the wake. Cumulative eigenvalues provide an insight on the turbulence kinetic energy and coherent structures. In this regards, Esau [38] showed that the Coriolis force produced a diminished effect on the flow under convective conditions compared to a neutrally stratified boundary layer flow using LES data. It was found that the most energetic POD modes accounted for up to 33% and 55% of the total TKE in the neutral and convective stratified flow, respectively. Shah and Bou-Zeid [34] showed the effect of buoyancy flux in the dominant POD modes and the energy balance. Their results quantified the streamwise rolling structures and the contribution of each scale to the energy balance and the momentum and scalar fluxes. Ali et al. [39] observed that the buoyancy force in the unstable case absorbs much of the perturbation induced by the wakes and that relatively large structures dominate the unstable and neutral cases. Contrarily, the buoyancy force within the stable regimes boost the velocity gradients and induces a larger change of wind veer with height. Therefore, the stable regime was found to strongly alter the structure of the background turbulent flow, and was fully dominated by the presence of turbines [2, 39].

The conditional sampling method introduced by Lu and Willmarth [40] provides a framework to interpret and detect coherent motion signatures, and to quantify the contributing nature of the Reynolds stress and scalar flux [41–43]. In the boundary layer, the signature of the coherent structures is marked with dominance of the fourth quadrant (sweep) of the shear stress near the wall. The above shear layer region is marked with ejection events (Q_2). In the atmospheric surface layer, it is shown that ejections and sweeps are strongly responsible for evaporation, sensible heat, and momentum fluxes [44]. The influence of thermal stratification on the ABL structure is also quantified by the quadrant analysis, where ejection and sweep events are associated with the coherent structures created and preserved by aerodynamic instability in the streamwise mean velocity profiles near the ground [45]. Also, these coherent structures have a significant role in momentum and scalar contribution to the fluxes. In the urban canopy, quadrant analysis combined with a joint probability density function was used to determine the frequency of particular events. Also, the sweep and ejection events were shown to exceed the other quadrants, especially with an increase in the aerodynamic resistance [46]. Using data collected via particle image velocimetry, quadrant analysis has been applied in turbulent boundary layers over rough walls, air-sea interaction aerodynamics, water waves, plant canopies, blowing-snow transport, and channel flow over a regular square bar roughness [46–59]. In roughness sublayer, canopy sublayer, and atmospheric surface layer experiments, ejection-sweep relationship for scalar and momentum transport are provided to show the contribution of heat flux and find some similarity in turbulent transport mechanisms [44, 60, 61]. In wind turbine wake flows, several studies have highlighted wake structures and quantified the mechanisms of entrainment and recovery processes of energy downstream of the turbines (cf. Hamilton et al. [62];Viestenz and Cal [7] and Kadum et al. [37]).

To characterize and classify events per momentum and scalar fluxes, quadrant analysis is used. Conditional averaging breaks up the signal of the fluctuating velocity components, pressure, and temperature into four quadrants based on the signs of the components. Therefore, the conditional averaging is determined as

$$\langle AB\rangle = \frac{1}{N}\sum_{t=1}^{N} \left(A_t(x,y,z)B_t(x,y,z)\ I_m\Big[A_t(x,y,z);B_t(x,y,z)\Big] \right), \tag{4}$$

where A and B represent the flux components, m presents the quadrant index (i.e., m =1, 2, 3, and 4), t is the time, and N is the total number of the snapshots. Further, I_m is a conditional function defined as

$$I_m\Big[A_t(x,y,z);B_t(x,y,z)\Big] = \begin{cases} 1 & \text{if } (A,B)\in m, \\ 0 & \text{otherwise.} \end{cases} \tag{5}$$

The corresponding quadrant combination for the scalars and momentum components are presented in Table I.

TABLE I. Four Quadrants Based on the Velocity Components and Scalar Signs.

Flux	Quadrant 1 ($Q1$)	Quadrant 2 ($Q2$)	Quadrant 3 ($Q3$)	Quadrant 4 ($Q4$)
$u'w'$	u^+w^+	u^-w^+	u^-w^-	u^+w^-
$u'p'$	u^+p^+	u^-p^+	u^-p^-	u^+p^-
$w'p'$	w^+p^+	w^+p^-	w^-p^-	w^-p^+
$u'\theta'$	$u^+\theta^+$	$u^-\theta^+$	$u^-\theta^-$	$u^+\theta^-$
$w'\theta'$	$w^+\theta^+$	$w^+\theta^-$	$w^-\theta^-$	$w^-\theta^+$

III. LARGE EDDY SIMULATION

The thermally stratified atmospheric flow of a realistic atmospheric diurnal cycle is simulated by time integrating the rotational form of the non-dimensional filtered incompressible Navier-Stokes equations, the continuity equation, and an advection-diffusion equation for temperature,

$$\begin{aligned} &\frac{\partial \tilde{u}_i}{\partial t} + \tilde{u}_j\left(\frac{\partial \tilde{u}_i}{\partial x_j} - \frac{\partial \tilde{u}_j}{\partial x_i}\right) = \\ &-\frac{1}{\rho}\frac{\partial p^*}{\partial x_i} - \frac{\partial \tilde{\tau}_{ij}}{\partial x_j} + g\left(\frac{\tilde{\theta}-\langle\tilde{\theta}\rangle}{\theta_0}\right)\delta_{i3} + F_c(\tilde{u}_2 - V_G)\delta_{i1} - F_c(\tilde{u}_1 - U_G)\delta_{i2} + f_i, \end{aligned} \tag{6}$$

$$\frac{\partial \tilde{u}_i}{\partial x_i} = 0, \tag{7}$$

$$\frac{\partial \tilde{\theta}}{\partial t} + \tilde{u}_j \frac{\partial \tilde{\theta}}{\partial x_j} = -\frac{\partial \pi_j}{\partial x_j}. \tag{8}$$

where, $\tilde{u}_i$ represents the LES-filtered velocity, the tilde ($\tilde{}$) represents the LES filtering operation at the grid-size (Δ), $\tilde{\theta}$ is the filtered potential temperature. The angle brackets $\langle\cdot\rangle$ represent a spatial average, and F_c is the Coriolis parameter. Here, the flow is driven via a height-independent geostrophic wind of $U_G = 9$ ms^{-1} in the streamwise direction and $V_G = -3$ ms^{-1} in the spanwise direction. The Boussinesq approximation is used to represent the influence of thermal stratification [1]. The filtered shear stress is introduced via τ_{ij}, and its deviatoric part is presented using the sub-grid Lagrangian scale-dependent model of Bou-Zeid et al. [63]. The sub-grid sensible heat flux π_j is modeled using the adjusted Lagrangian scale-dependent model for scalars [64]. The approach presented in [65] is applied here to model the actuator disk with rotation and yaw-alignment (ADM-RY). The thrust and drag coefficients used in this study were 1.333 and 0.8, respectively, representative of a standard wind turbine [5]. The wind turbines are readjusted to the incoming wind every 10 minutes following the same procedures presented in [66, 67]. In the LES of atmospheric flows, the viscous effects are generally neglected and the differential equations are discretized via a pseudo-spectral discretization Moeng [68] and Albertson and Parlange [69]. The equations are dealiased using the 3/2-rule [70], and time-integrated using a second-order Adams-Bashforth scheme. The numerical algorithm is fully parallelized using the Message-Passing Interface (MPI). Additional details about the LES code can be found in [2, 39].

The boundary condition used in this study are at the top of the domain consists on a zero flux for momentum and temperature. At the bottom, a non-slip condition is applied for the vertical velocity. Alternatively, an equivalent shear stress is imposed at the first grid point above the surface for the horizontal momentum components and temperature. This shear stress is characterized via the traditional log-law including the effects of stratification [63, 71, 72],

$$\tau_{i,3}(x, y, z_1) = -\left[\frac{\kappa\sqrt{\left(\tilde{u}_1^2 + \tilde{u}_2^2\right)}}{ln(\frac{z_1}{z_0}) + \psi_m(\frac{z_1}{L})}\right]^2 n_i. \tag{9}$$

Here κ is the Von Kármán constant which is equal to 0.4. The z_1 is the height of the first staggered grid point, where the horizontal velocity components are computed ($z_1 = \Delta z/2$) and the shear stress is imposed. More, z_0 is the ground surface roughness, which is imposed as homogeneous with a value of $z_0 = 3 \cdot 10^{-5} z_i$, where $z_i = 1,000$ m is the initial boundary layer height used as a normalizing length scale. In Equation (9), n_i is a unitary directional vector, $n_i = \tilde{u}_i/\sqrt{\tilde{u}_1^2 + \tilde{u}_2^2}$, where i indicates either of the horizontal plane-parallel directions ($i = 1, 2$). The vertical derivatives of the horizontal velocities are also parametrized at the first grid point z_1 [73],

$$\partial_3 \tilde{u}_i(x, y, z_1) = \frac{\sqrt{\tau}}{\kappa z} n_i, \tag{10}$$

with $\tau = \sqrt{\tau_{1,3}^2 + \tau_{2,3}^2}$. To integrate the potential temperature, Equation (8), a time-varying surface temperature is imposed, from which the surface sensible heat flux is computed using Monin-Obukhov's similarity theory and imposed at the first staggered grid-point,

$$H_s(x, y, z_1) = \frac{\kappa^2[\theta_s - \tilde{\theta}(x, y, z_1)]\left(\sqrt{\tilde{u}_1^2 + \tilde{u}_2^2}\right)}{\left[ln(\frac{z_1}{z_0}) + \psi_m(\frac{z_1}{L})\right]\left[ln(\frac{z_1}{z_{0,h}}) + \psi_h(\frac{z_1}{L})\right]}. \tag{11}$$

In this case, $z_{0,h}$ represents the scalar surface roughness, which is taken to be one-tenth of the momentum surface roughness $z_{0,h} = z_0/10$, see Brutsaert et al. [74]. The stability correction functions $\psi(z_1/L)$ implemented are also those of Brutsaert [75]. For the unstable case, the stability correction functions are given by [65]

$$\psi_m(z/L) = \begin{cases} \ln(a - z/L) - 3b(z/L)^{1/3} + \frac{ba^{1/3}}{2}\ln\left[\frac{(1+x)^2}{1-x+x^2}\right] + & \\ \sqrt{3}ba^{1/3}\tan^{-1}\left[(2x-1)/\sqrt{3}\right] + \psi_0 & \text{for } z/L \le b^{-3} \\ \psi_m(b^{-3}) & \text{for } z/L > b^{-3}, \end{cases} \tag{12}$$

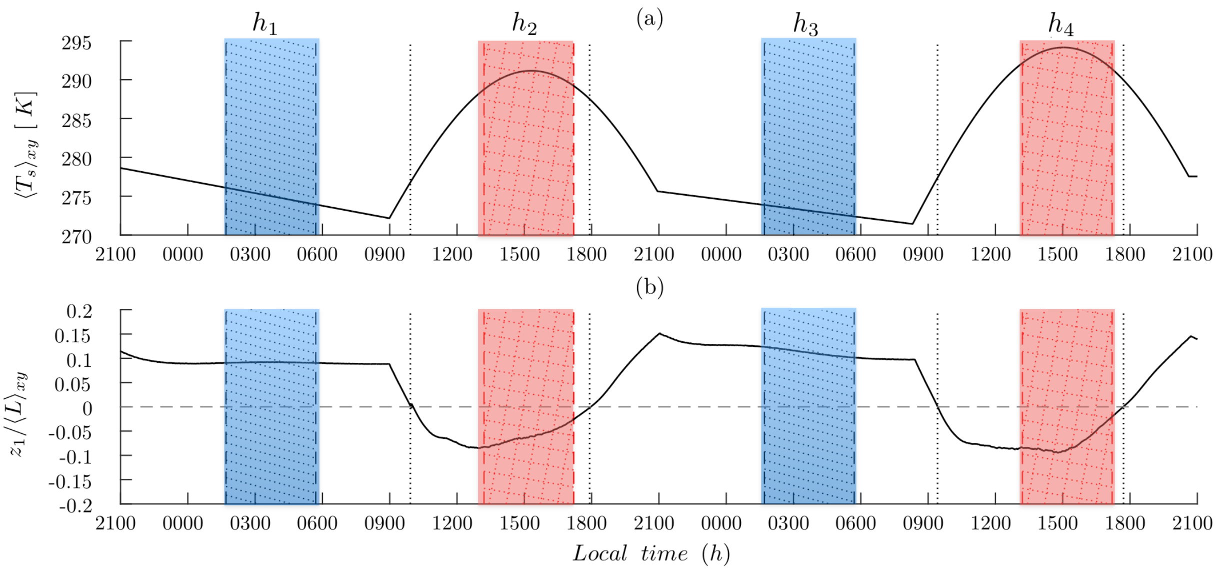

FIG. 1. (a) The spatially averaged and time-dependent imposed temperature at the surface of the domain $\langle T_s \rangle_{xy}$ in Kelvin, and (b) the normalized stability parameter, $z_1/\langle L \rangle_{xy}$, where ($z_1 = \Delta z/2$) is the height of the first grid-point and L is the Monin-Obukhov length, as a function of time. Note that $\langle \cdot \rangle_{xy}$ indicates the spatial average operation, in the streamwise and spanwise direction.

and

$$\psi_h = [(1-d)/n] \ln \left[(c + y^n/c\right], \tag{13}$$

where $x = (-z/La)^{1/3}$, and $\psi_0 = (-\ln a + \sqrt{3} b a^{1/3} \pi/6)$. For the stable scenario, the stability correction functions are implemented as

$$\psi_m = -a \ln \left[y/L + (1 + (z/L)^b)^{1/b}\right], \tag{14}$$

$$\psi_h = -c \ln \left[y/L + (1 + (z/L)^d)^{1/d}\right]. \tag{15}$$

The corresponding constants implemented for the stable case are $a = 6.1$, $b = 2.5$, $c = 5.3$, and $d = 1.1$, and for the unstable cases are $a = 0.33$, $b = 0.41$, $c = 0.33$,$d = 0.057$ and $n = 0.78$.

The temporal evolution of the surface temperature was extracted from a selected period (October 22 and 23, *see* Figure 1) of the Cooperative Atmosphere-Surface Exchange Study (CASES-99) that measured in Len, Kansas, from October 1st to 31st, 1999 [76]. In the present study, a total of 48 hours (starting at 2100 local time on the 22nd of October) is extracted. A few selected four-hour study periods are taken into account to compute turbulence statistics. These periods are highlighted in Figure 1 as h_1 and h_3 (stable case), and h_2 and h_4 (unstable case). Time periods h_1 and h_3 constitute the times between 01:45 and 05:45, and p2 and p4 range between 13:15 and 17:15. The numerical domain has a size of $(2\pi \times \pi \times 3)z_i$. A uniform numerical grid of $256 \times 128 \times 384$ points is chosen, providing a uniform grid resolution of $\Delta y = \Delta x = 24.5$ m and $\Delta z = 7.8$ m. The wind farm cases each consist of eight rows and six columns of turbines. The spacing of the turbines is set to be $\sim 7D$ and $\sim 5D$ in the streamwise (s_x) and spanwise (s_y) directions, respectively, where D is the wind turbine rotor diameter, set equal to 100 m.

IV. RESULTS

The mean velocity and Reynolds shear stresses for unstable and stable scenarios are presented in terms of their contribution to the overall energy budget. Thereafter, particular terms from the turbulence kinetic energy budget terms are introduced and contrasted against one another, and the second- and third-order correlations of the velocity and scalars are provided. Finally, the quadrant analysis for momentum and scalar flux is detailed.

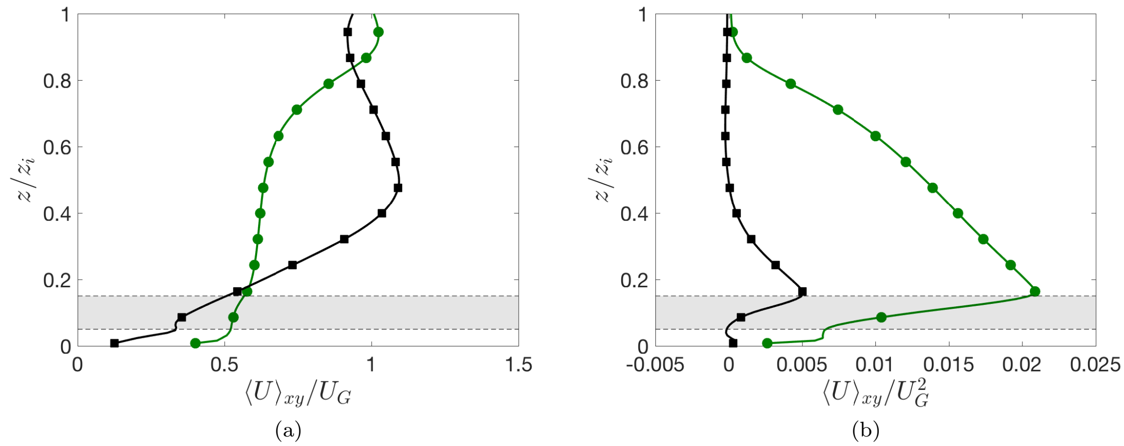

FIG. 2. (a) The vertical profiles of mean wind speed, $\langle U \rangle_{x,y}$, normalized with U_G, and (b) the vertical shear, $\langle \tau \rangle_{x,y}$, normalized with U_G^2, for the different atmospheric stability regimes: Unstable case ( ), and stable case (■). The shaded area represents the location of the rotor.

A. Mean Flow Statistics

Figure 2 illustrates time- and spatially-averaged normalized vertical profiles of mean wind speed, $\langle U \rangle_{xy}$, and vertical mean shear stress, $\langle \tau \rangle_{xy}$. The spatial average operation is presented as $\langle \cdot \rangle_{x,y}$, in the streamwise direction, spanwise direction, and the time average during the four-hour time period marked in Figure 1. The vertical swept area of the wind turbine rotor disk is delineated as a shaded grey region between $z = 0.05z_i$ and $z = 0.15z_i$. This figure intends to validate the current simulations by reproducing the mean characteristics of the wind turbine array boundary layer (WTABL) flow [6, 8, 15]. In the results, the geostrophic wind speed (U_G) and initial boundary layer height (z_i) are used to normalization purpose. In regards to the mean flow, in Figure 2(a) the stable case exhibits a sharper gradient near the surface, with a stronger momentum deficit within the rotor-disk layer. A Low-level jet is distinguished at a height of $z \approx 0.4z_i$ in the wind farm under stably stratified conditions, as a result of the decrease in turbulent mixing and decoupling of the surface layer from the outer boundary layer [1]. In contrast, the velocity profiles for the unstable case displays a strong gradient near the surface and a well-developed profile above. The changes in wind velocity by the time-varying thermal stratification impact the harvested power. The wind farm under unstable stratification produces a power of twice the magnitude than that produced under stable condition [77]. This is partly due to the vertical displacement of the low-level jet in very large wind farms. Figure 2(b) presents the normalized Reynolds shear stress, $\langle \tau/U_G^2 \rangle_{xy}$ for the considered cases. In the stable case, the normalized Reynolds shear stress shows enhanced gradient across the rotor layer. The maximum vertical shear stress is observed at the top tip of the rotor. Similarly, under an unstable condition, the wind plant experiences a significant increase in the shear stress due to the positive buoyancy flux enhancing turbulent mixing and the overall turbulence kinetic energy.

B. Turbulence Kinetic Energy Budget

Figure 3 shows the TKE budget terms for the unstable and stable cases. It should be noticed that while grouping the different terms, the local storage or tendency of turbulent kinetic energy ($\partial \overline{e}/\partial t$) has not been taken into account. Consequently, the residual of the turbulence kinetic energy budget will represent the local storage of TKE. The production term (PR) has been presented individually for each of the different contributions to recognize how the TKE is produced for the different stability conditions as described in the theory section. TKE budget terms are normalized with the diameter of the rotor (D) and the streamwise component of the geostrophic velocity (U_G^3). Thus, the positive and negative TKE means that the source and sink of the perturbation in the flow field, respectively. The TKE budget of the unstable case is presented in Figure 3(a). The magnitude of the dissipation term is increased near the surface as a result of the pronounced energy transfer at this location, where the TKE production and buoyancy, respectively, are most significant. The dissipation budget shows a gradual decrease in the region from the surface to the bottom tip. The change in the dissipation within the swept area of the rotor is slower than that below the bottom tip. Above the rotor, dissipation further decreases, and becomes zero at the top of the boundary layer. Turbulent transport is affected by coherent eddies over the entire domain and is considered as the footprint of both mixing

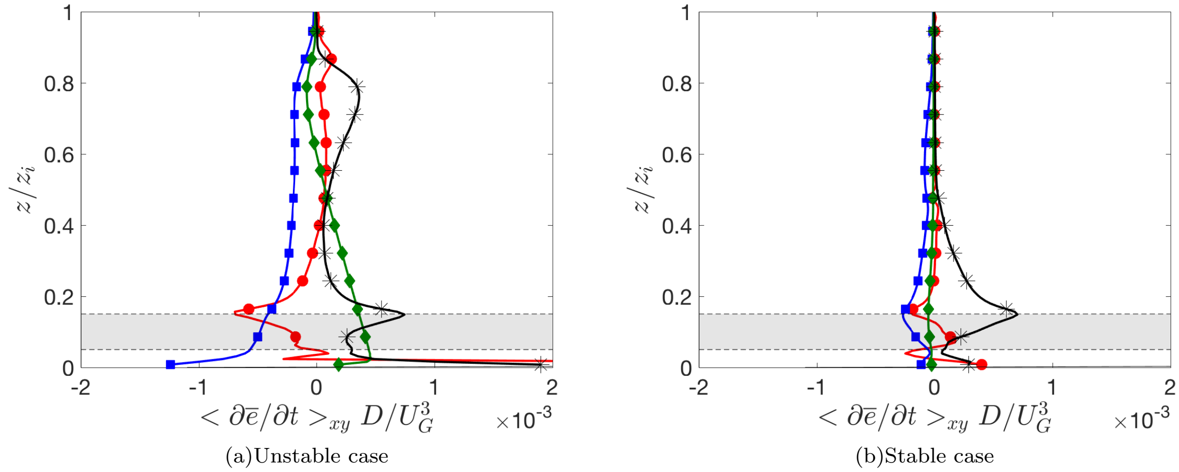

FIG. 3. Vertical profiles of the TKE budget terms for the unstable (a), stable (b) cases. The lateral brackets $\langle\cdot\rangle_{xy}$ indicate the planar average operation in $x-y$ planes as a function of height (z) normalized by the initial boundary layer thickness. The TKE budget terms are normalized by the U_G^3/D. The markers are the dissipation (■), transport ( ), production by buoyancy PR_b (♦), and shear production PR_s ($*$). The shaded area represents the location of the rotor.

layers and wind turbines. The transport of the TKE experiences a decrease below the bottom tip, where it becomes a sink of turbulence. In the swept area of the rotor, the transport term increase in the negative direction, reaching the maximum at the top tip (maximum sink). Thereafter, the transport term becomes marginal above the LLJ location until the height of $0.8z_i$, where an inflection point is present. This shows an increase followed by an attenuation. The buoyancy term increases above the surface and then begins to decrease below the bottom tip. The inversion in the buoyancy sign occurs at $0.6z_i$. Thereafter, the buoyancy decreases and becomes marginal at the uppermost layers of the ABL. Turbulence production is maximum at the top tip of the rotor area and at the level at which the buoyancy and the transport terms are minimum. Shear production is large near the surface, where it is approximately in balance with the transport term; both are leading-order terms in the TKE budget. The rapid decrease of the production above the rotor area is a consequence of the rapid depletion of the Reynolds stresses.

The TKE budget for the stable case is presented in Figure 3(b). Turbulence dissipation shows a gradual decrease from the surface to the bottom tip, increasing across the swept area of the rotor, and finally decreasing above the top tip to eventually reach zero at the top of the boundary layer. The transport of the TKE experiences a decrease in magnitude above the bottom tip and becomes negative above the top tip, switching signs above the swept area. Buoyancy increases above the surface and then starts decreasing below the bottom tip. The buoyancy term acts as a sink of TKE together with the dissipation term. Turbulence production is maximized at the top tip, where minimum values of transport and dissipation are observed. Comparing the stable and unstable cases reveals that the order of magnitude of the unstable terms is much greater than that presented during the stable case. Based on the thermal stability used in this study, the variability of the budget terms in the rotor swept area is smaller in the stable case, indicating that the thermal stability suppresses the wind turbine effect.

Although this study is related to wind energy, various observations above are consistent with classical turbulent boundary layers. For example, Skåre and Krogstad [78], Krogstad and Skåre [79] showed that there are two peaks in the turbulent production one close to the surface and one in the outer layer. Also, they reported that there are three peaks along with the the turbulent transport (positive-negative-positive), especially in the adverse pressure gradient. Thus, the dissipation and viscous diffusion are very large close to the surface [80]. For the stable atmospheric boundary layer, Babić and Rotach [81] found that within the roughness surface layer the mechanical production is larger than the dissipation and the buoyancy destruction. In other words, the transport becomes a sink of turbulence, where the TKE is transported upward at the wind turbine swept area. The energy balance among the TKE budget terms is the key to control the power harvested by the rotors. The potential impact of distinctive flow dynamics on the structure of wind turbines and wind farm power fluctuations is introduced in different studies. For example, Tobin et al. [82] unraveled the structure of the power output fluctuations by introducing a basis for the prediction of power output in the power spectral domain. Liu et al. [83] found that the spectra of the power fluctuations contains two power-law trends distinct between the relatively low- and high-frequency ranges due to the scale interaction, and the advection between turbine pairs. Thus, Bossuyt et al. [84] used the wavenumber-frequency spectrum to model the fluctuations in power output as a function of wind farm layout and inflow turbulence properties of the wind.

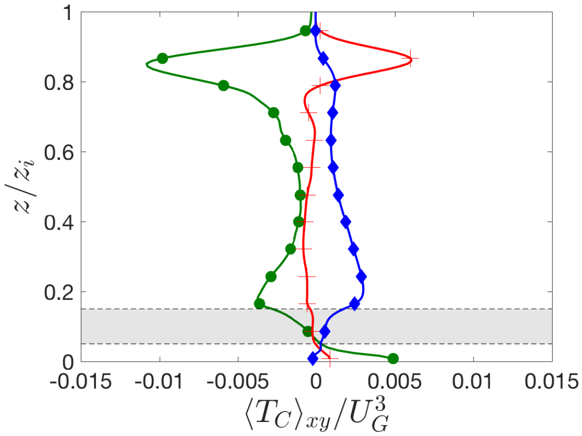

(a)Unstable case

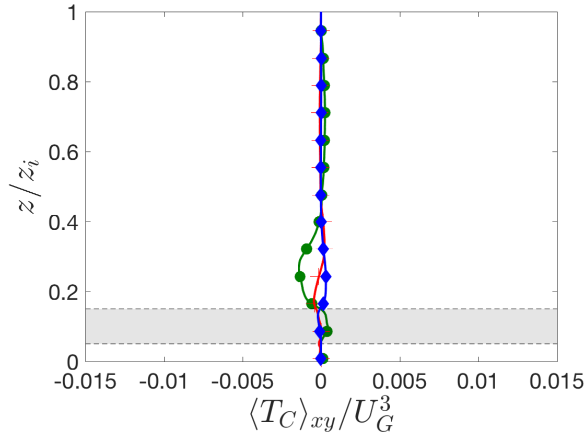

(b)Stable case

FIG. 4. Triple velocity correlation T_C related to the streamwise normal Reynolds stress for the unstable (a), stable (b) cases. The markers are the u'^3 ( ), u'^2v' (+), and u'^2w' (♦). The triple correlations are normalized by the U_G^3.

C. Triple Correlations

Figures 4 through 6 display the vertical profiles of the horizontally-averaged triple correlations of the velocity components. The triple correlations represent the turbulent convection, and are a part of the diffusion term of the transport equation [85]. The triple correlation considers the Reynolds stresses as a flux that is responsible for the redistribution of turbulence kinetic energy from the region above the wind plant to the region below. Thus, these correlations are the basis of turbulence closure models. For example, in a model proposed by Lumley, it is assumed that the triple correlation is balanced by the correlation between the velocity and pressure [85]. The current results show that the change in the streamwise component is compensated via the variation in wall-normal and spanwise components. The same observation is shown in Kadum et al. [37]. Further, in the unstable case shown in Figure 4, the variance of $\langle u'^3 \rangle$ quickly becomes more negative above the bottom tip, bounded within the swept area of the rotor. The variance starts decreasing above the rotor and becomes constant at the region of $z/D \in [0.2 - 0.6]$. Thereafter, the $\langle u'^3 \rangle$ increases in the negative direction until reaching the inflection point at $z/D = 0.8$ that changes the sign direction of the correlation. The variances of $\langle u'^2v' \rangle$ and $\langle u'^2w \rangle$ shown in Figure 4 display the opposite behavior, for example $\langle u'^2w' \rangle$ increases in the positive direction above the ground, and $\langle u'^2v' \rangle$ increases in the higher layer of the ABL. These observations confirm the applicability of Lumley's model if one considers the redistribution of the TKE through the normal stresses. The variation in the correlation under the stable case is minor, especially for the wall-normal and spanwise components. Indicating that the streamwise normal stress are dominant, and the turbulence state under stable condition tends to be one-component turbulence. The same conclusions are observed in Ali et al. [2]. In contrast, under the unstable scenario the turbulence state displays a contribution of three components of the velocity, and the weight of the contribution determines the turbulence state to be prolate, oblate, or axisymmetric, etc. The triple correlation is a third moment that displays multiple distinct peaks as shown in Figures 5 and 6. The presented third moments are asymmetric about zero except $\langle u'^3 \rangle$, meaning that the flow is skewed in different directions based on the location above the surface. For example, very large amplitude variance of $\langle v'^3 \rangle$ and $\langle w'^2v' \rangle$ are skewed to the positive and negative side, respectively, thus indicating that the imbalance determines the net value of the triple correlations.

Meyers and Baldocchi [86] studied the triple velocity correlations of a deciduous forest. They observed that the large vertical gradients are observed in the upper canopy. Also, they reported that the $\langle u'^2w' \rangle$, $\langle v'^2w' \rangle$, and $\langle w'^3 \rangle$ are negative due to that the canopy acts as a sink for turbulent structures. Here, the later values are positive as shown in the above Figures hence indicative of an important difference between the wind turbine canopy and the vegetated canopy. These results show that the turbines represent a source of turbulent motions and a sink for momentum.

D. Velocity-Pressure Covariance

Figure 7 presents the covariance of the fluctuating velocity components and pressure. For the stable case, a positive covariance between the streamwise velocity and pressure is observed at the wake perturbation region and above the

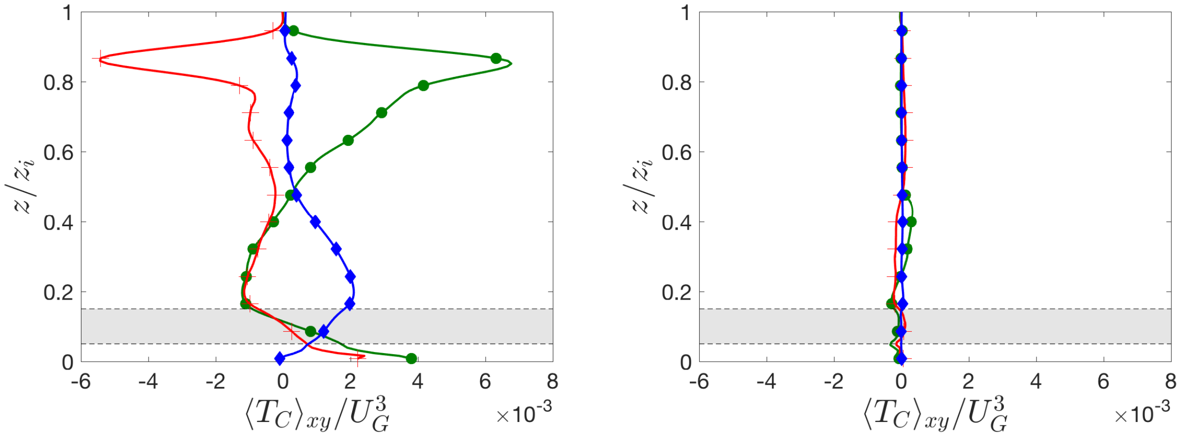

(a)Unstable case (b)Stable case

FIG. 5. Triple velocity correlation T_C related to the spanwise normal Reynolds stress for the unstable (a), stable (b) cases. The markers are the v'^3 ( ), v'^2u' (+),and v'^2w' (♦). The triple correlations are normalized by the U_G^3.

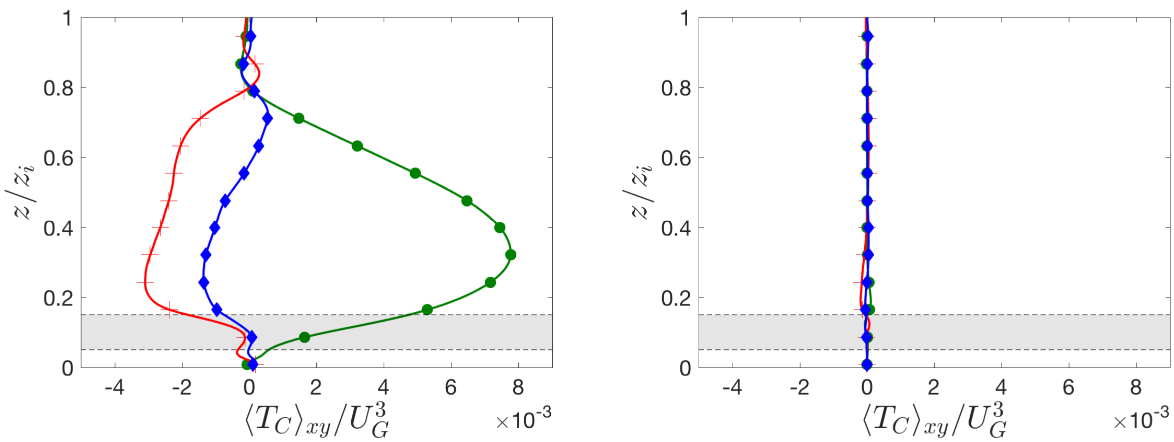

(a)Unstable case (b)Stable case

FIG. 6. Triple velocity correlation T_C related to the wall-normal Reynolds stress for the unstable (a), stable (b) cases. The markers are the w'^3 ( ), w'^2u' (+), and w'^2v' (♦). The triple correlations are normalized by the U_G^3.

shear layer. Due to the drag of the rotors the covariance is reduced in the swept area. A negative covariance is noticed at upper levels of the ABL as a consequence of pressure deceleration. The covariance exhibits a maximum at the top of the unstable layer. For $\langle v'p' \rangle$, the correlation is always positive. The same trend is observed for $\langle w'p' \rangle$ at the region above $0.6z_i$. Below this region, the covariance $\langle w'p' \rangle$ is negative, thus indicating that u' and w' are inherently negatively correlated, and the high-momentum fluid is directed downward onto the wake region. Based on the above discussion, a major loss in energy is associated with the streamwise fluctuation, mainly absorbed by the spanwise component at least in the wake region.

For the stable case, a strong positive covariance is shown near the surface due to the significant gradient in the velocity component. The location of the low-level jet separates the covariance of the streamwise velocity and pressure into two regions; below the LLJ is positive and above is negative. The higher layers of the flow display approximately a constant negative covariance. The spanwise component of the velocity is uncorrelated with the pressure. The covariance of the wall-normal component and pressure displays a change in sign at the bottom tip and keeps exhibiting a negative value for all regions above the rotor. The shear layer above the wind turbine absorbs the energy from the streamwise component and redistributes it to the wall-normal and spanwise directions. Higher layers of the domain show the opposite; wall-normal and spanwise components feed the streamwise component of the Reynolds stress tensor. Linear gravity theory pointed out that the $\langle w'p' \rangle$ is equal the the upward flux of wave energy [1]; meaning that the pressure correlation drains the turbulence energy out of the boundary layer, where it is vertically propagated

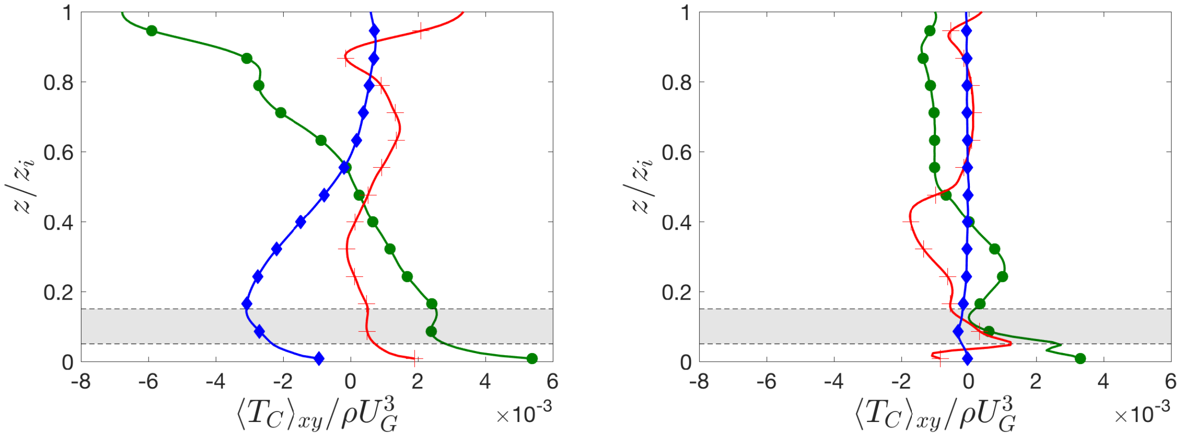

(a)Unstable case (b)Stable case

FIG. 7. Pressure-velocity covariance T_C for the unstable (a), stable (b) cases. The markers are the $u'p'$ ( ), $v'p'$ (+), and $w'p'$ (♦). The profiles are normalized by the ρU_G^3.

and dissipated in the form of gravity waves.

E. Velocity-Temperature Covariance

Changes in the heat flux and stratification regimes significantly affect the turbulence state and lead to a decay or increase in the flow variability. Figure 8 presents the covariance of the velocity and temperature for the considered cases. The covariance of the streamwise velocity and temperature displays a negative value adjacent to the surface till $0.7z_i$. The maximum positive covariance is noticed at $0.8z_i$. The covariance of the wall-normal velocity and temperature displays an opposite trend of $\langle u'\theta' \rangle$. The unstable case shows positive turbulent heat flux $\langle w'\theta' \rangle$ adjacent to the surface, extending up to $0.6z_i$, where it becomes zero. Thereafter, the heat flux displays small negative values which are due to entrainment at the top of the convective boundary layer. During the stably stratified period, the profile of heat flux $\langle w'\theta' \rangle$ presents sharper differences especially near the surface and within the rotor-disk region. The flux shows a sharp gradient below the rotor and the zero-flux limit is reached near the $0.6z_i$ height, illustrating the induced growth of the boundary layer as a result of the enhanced mixing by the presence of the turbines. At upper levels, the heat flux $\langle w'\theta' \rangle$ tends to zero, in contrast to $\langle u'\theta' \rangle$ and $\langle v'\theta' \rangle$ which show small values that can be neglected when compared to $\langle w'\theta' \rangle$. Mironov and Sullivan [87] showed that in the stable boundary layer the turbulent transport is small, with the exception of the case where the surface presents thermal heterogeneity, and the $\langle u'\theta' \rangle$ and $\langle v'\theta' \rangle$ are positive near the surface. Similar observations are also found in the current analysis.

F. Triple Correlation of the Velocity and Temperature

Figure 9 presents triple correlations of the velocity and temperature for the considered cases. The triple correlations between the velocity and temperature are a part of the heat flux budget, which are included in the flux transport term [1]. The correlation $\langle u'^2\theta' \rangle$ is negative for both cases. The unstable case displays higher triple correlation than the stable case. The maximum value is found near the LLJ location in the stable case, and at the $z = z_i$ of the unstable domain. The correlation $\langle u'v'\theta' \rangle$ tends to be constant in the region $0.2 \leq z/z_i \leq 0.8$. Then the correlation becomes positive and turns to zero at the top of the boundary layer. The stable case shows a steep gradient in the correlation especially in the rotor area and above, although the correlation sign does not change. The low-level jet changes the sign of the correlation in the stable case. The location $0.8z_i$ exhibits an inflection point, where above this point the correlation begins to decrease and becomes null at the top of the boundary layer. The correlation $\langle u'w'\theta' \rangle$ displays the same trend of the Reynolds shear stress, where it tends to become linear with height over most of the flow layer. It is also noteworthy that the correlation $\langle u'w'\theta' \rangle$ decreases in the entrainment zone. The correlation $\langle w'^2\theta' \rangle$ reveals an opposite trend of the correlation $\langle u'w'\theta' \rangle$. Zhou et al. [88] studied the temperature flux budget in a convective boundary layer and showed that the gradient of the $\langle w'^2\theta' \rangle$ is negative near the surface and becomes null below the

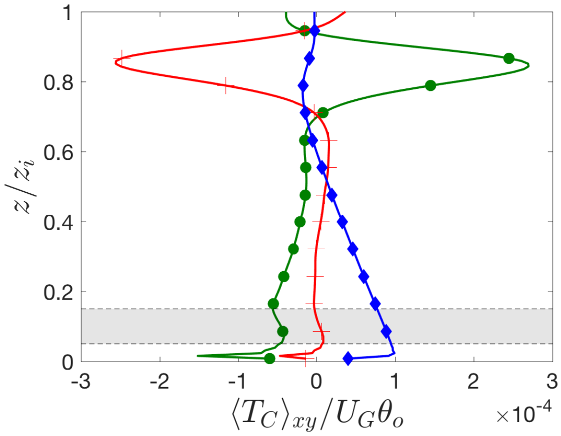

(a)Unstable case

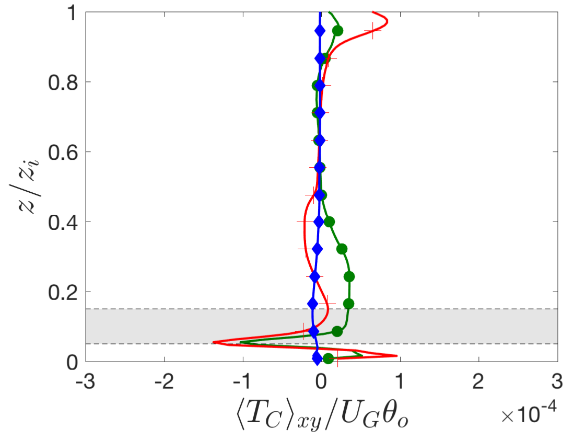

(b)Stable case

FIG. 8. Temperature-velocity covariance T_C for the unstable (a), stable (b) cases. The markers are the $u'\theta'$ ( ), $v'\theta'$ (+),and $w'\theta'$ (♦). The profiles are normalized by the U_G and θ_o.

z_i level. Here, the same observation is shown near the surface. The sign of the gradient is changed above the the rotor due to the changes in the preferential direction of the turbulence. The stable correlation of $\langle v'^2\theta'\rangle$ exhibits more alternating behavior than the unstable case. Effects of the bottom tip and hub height are observed to reduce the variation. Nevertheless, the correlation $\langle v'^2\theta'\rangle$ tends to be null at the LLJ location and the boundary-layer thickness. The unstable case decreases and becomes zero at the higher layer of the flow. The correlation $\langle v'w'\theta'\rangle$ also displays the same trend of $\langle w'\theta'\rangle$ for the stable case, whereas the stable case is constant over most of the flow layers. For both unstable and stable cases, only the triple correlation $\langle u'w'\theta'\rangle$ tends to zero at upper levels as a consequence of the depletion of the Reynolds stress.

G. The Reduced Turbulence Kinetic Energy Budget

Stating with the assumptions including the essential information of the TKE distributions in the wind farm. The assumptions used to reduce the TKE budget are that the streamwise mean velocity is major and a function of z. The other two components of the mean velocities are zero. The gradient with z is larger than the gradient with respect to the other coordinates ($\frac{\partial}{\partial z} >> \frac{\partial}{\partial x}$ and $\frac{\partial}{\partial y}$). The reduced form includes that the contributions of the shear and buoyancy production mechanisms, and imbalance between production and dissipation. The reduced form of the TKE budget can be written as

$$R = \frac{g}{\overline{\theta}}(\overline{w'\theta'}) - \overline{u'w'}\frac{\partial U}{\partial z} - \frac{\partial(\overline{w'\overline{e}})}{\partial z} - \frac{1}{\overline{\rho}}\frac{\partial(\overline{w'p'})}{\partial z} + \epsilon_f, \tag{16}$$

where R is the residual. Figure 10 presents the reduced TKE budget for unstable and stable cases. This figure points out the remarkable similarity with the full budget shown in Figure 3. However, this in not the case in the region near the surface, where the contribution of the gradient is large, which affects the accuracy of the transport term. Also, the swept area of the turbine shows a variation between the full and the reduced form of the transport term as a result of neglecting the contribution of the $\frac{\partial(\overline{u'\overline{e}})}{\partial x}$ and $\frac{\partial(\overline{v'\overline{e}})}{\partial y}$ in this region. Another observation that can be highlighted is that shear production is the dominant mechanism in the stable case, and the imbalance or the residual fills the variation with the dissipation and transport terms. In contrast, the swept area of the unstable case shows a balance between the shear production and transport, and a balance between the buoyancy and dissipation. Meaning that the total production scales are split into two parts: one dissipating into small scales and the other being transported by pressure diffusion and triple correlations to other regions. From the vertical profiles, a large fraction of production is transported elsewhere, especially in the swept area of the rotors. This point can answer the question highlighted in the introduction section about controlling the production term based on the remaining terms of the TKE budget. In the unstable case, the transport term $\frac{\partial(\overline{w'\overline{e}})}{\partial z}$ is enough to control the production. In contrast, in the stable case the

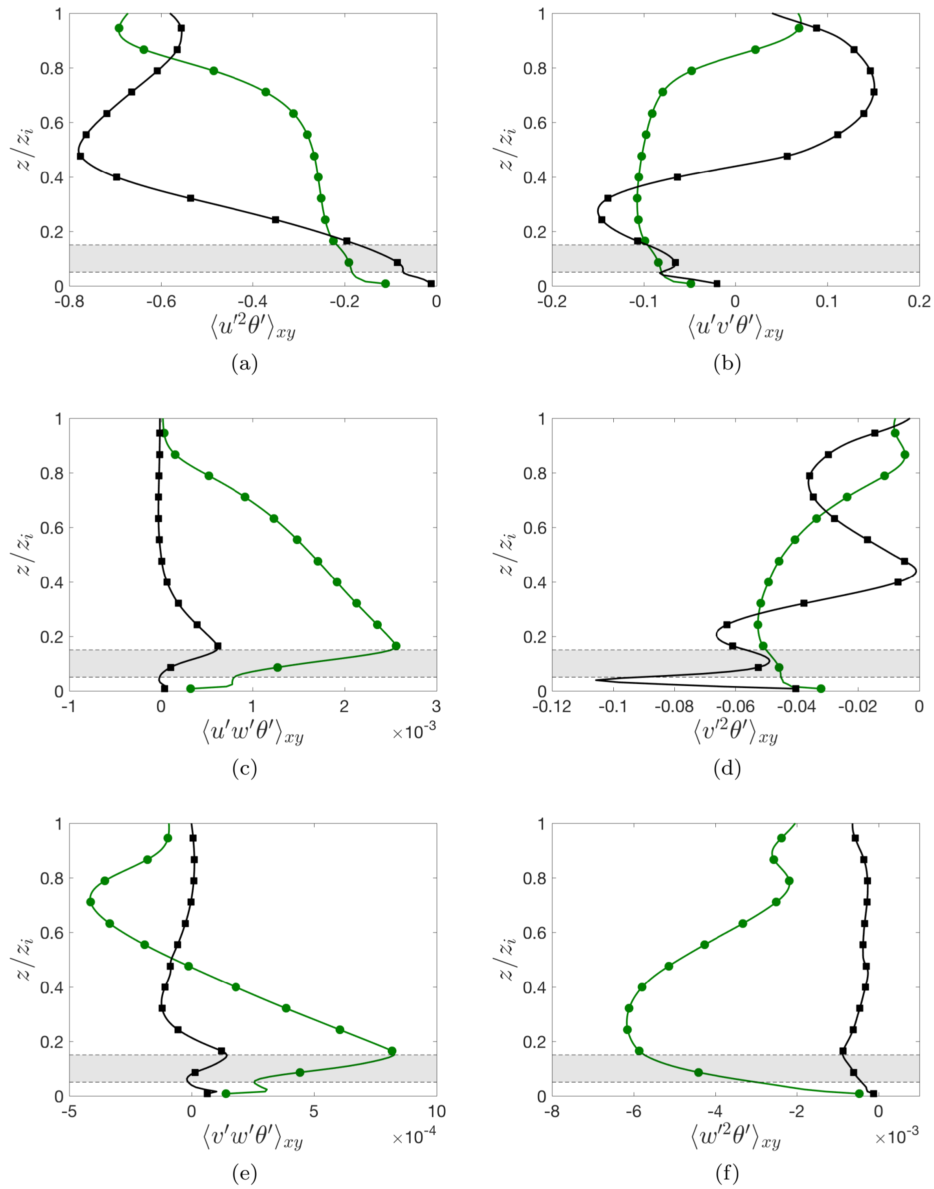

FIG. 9. Triple correlations of the temperature-velocity for unstable ( ) and stable cases (■). The velocities and temperature are normalized by U_G and θ_o, respectively.

transport and dissipation are not enough to destroy the TKE production. The variation in the magnitude presents a storage of TKE through the diurnal cycle.

V. QUADRANT ANALYSIS

Quadrant analysis with respect to momentum and scalar flux is performed and presented in this section to interpret and detect coherent motion signature. Figure 11 presents the quadrants of the momentum flux (Reynolds shear stress) for a $x - z$ plane that crosses through the center of the rotor disk. For the unstable case, the Reynolds shear stress-based contribution of sweep and ejection events exceed those in quadrants 1 and 3. Results show that a maximum for ejections is found just at the top tip and above, while a maximum for sweeps is observed at the top tip. Both of these maxima for ejections and sweeps contribute to the vertical kinetic energy flux. The patterns found in the Reynolds shear stresses in regards to ejection events show a preference for vertical expansion and interaction with the higher layers of the atmosphere. Thus, the contribution of the ejections to the Reynolds stress is greater than that

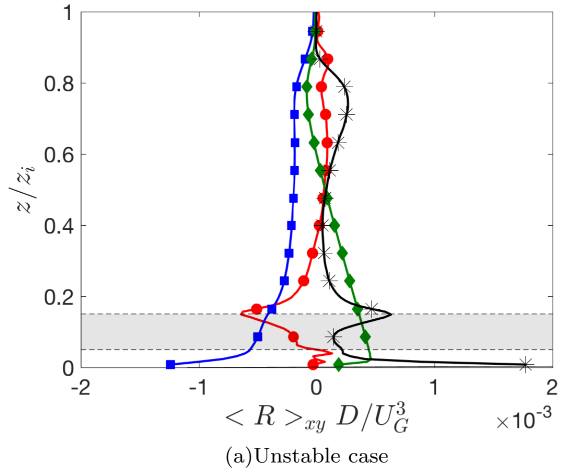

FIG. 10. Vertical profiles of the reduced TKE budget for the unstable (a), stable (b) cases. The lateral brackets $\langle\cdot\rangle_{xy}$ indicate the planar average operation in $x-y$ planes as a function of height (z) normalized by the initial boundary layer thickness. The TKE budget terms are normalized by the U_G^3/D. Markers define as in figure 3.

of the sweeps. Accordingly, the region of the wakes below the top tip and higher layer of the flow show a substantial contribution in quadrants 1 and 3. Indicating that the coherent structures generated by instabilities arise from the large vertical Reynolds shear stress near the wake-ABL interface. For the stable case, the contribution in quadrants 2 and 4 is dominant in comparison with that of quadrants 1 and 3. The wake and shear layer above the turbines are marked with maximum sweep and ejection and the wake interaction between the turbines is clear in these quadrants. The low-level jet location is marked with minimum shear stress fractions. The region just above the low-level jet has a constant stress. Thus, the sum of the shear stress is constant with height, where the increase in the positive stress producing ejections and sweeps is accompanied by greater negative stress producing events in quadrants 1 and 3. The region near the surface displays low contribution of the stress and highlights the interaction with flow below the top tip. The conditional sampling shows that flow has a uniform layer that carries a unified stress fraction, confirming that thermal stratification has a big influence on the suppression of the mechanical stress. The flow above the canopy is distinct from the wake region flow, where the direction of the fluxes by the sweeps and ejections is opposite to those in the undisturbed flow (above the shear layer), indicating that there is minimal mixing flux between the wake region and the flow above. The coherent exchange in the stable case is less than that with unstable stratification, where the flow is subjected to heterogeneously distributed sources and sinks of flow filed and scalars. The flux transported into the wake region is strongly dependent on the sign of the buoyancy. The upward-directed flux during the unstable period increases the energy exchange in the upper region of the wake, while the dramatic reduction in the flux is observed in the lower part of the wake. During the stable period when the flux is directed downward, the magnitude of the fluxes is significantly reduced. Differences in the energy exchange with height during the unstable and stable conditions indicate changes in wake morphology with thermal stratification.

Figure 12 shows the quadrant analysis for the scalar flux based on the streamwise velocity component and pressure $\langle u'p'\rangle$, for the considered plane. The flux $\langle u'p'\rangle$ can be interpreted as the force that is advected via the streamwise component of the velocity. The positive and negative fluctuating pressure can be explained as tension and compression forces, respectively. For the unstable case, the four quadrants have a significant weight on the total contribution of the scalar flux. In the wake region, the first and third quadrants are maximum, while the higher layer sweep event exceeds those in the other quadrants. The same observations are also found for the stable case. The perturbations near the surface are marked with maximum contribution in the first and third quadrants. Internal boundary layers reflect the impact of the wind turbine rotors and act to decouple the near-wall flow from the flow above the rotors. Above the wake perturbation layers and entrainment regions, the flow shows an increase in the contribution of the sweep events, as a result of accelerating flow in the unperturbed higher layers. Regions of high shear at the boundaries of each wake lead to increased production of turbulent kinetic energy and greater turbulence anisotropy. The rolling structures are observed at higher layers of the domain, where they are marked with maximum sweep events, although they show a moderate contribution of the other quadrants. Low-level jet structures help to identify structures internal to the wakes, and take on average values of momentum transport throughout the four quadrants. For both stable and unstable cases, the wake region is dominant with negative pressure (compression) as a result of the flow and turbine body interaction, where the turbines are stagnation points. Pressure fluctuations decrease when the flow moves far

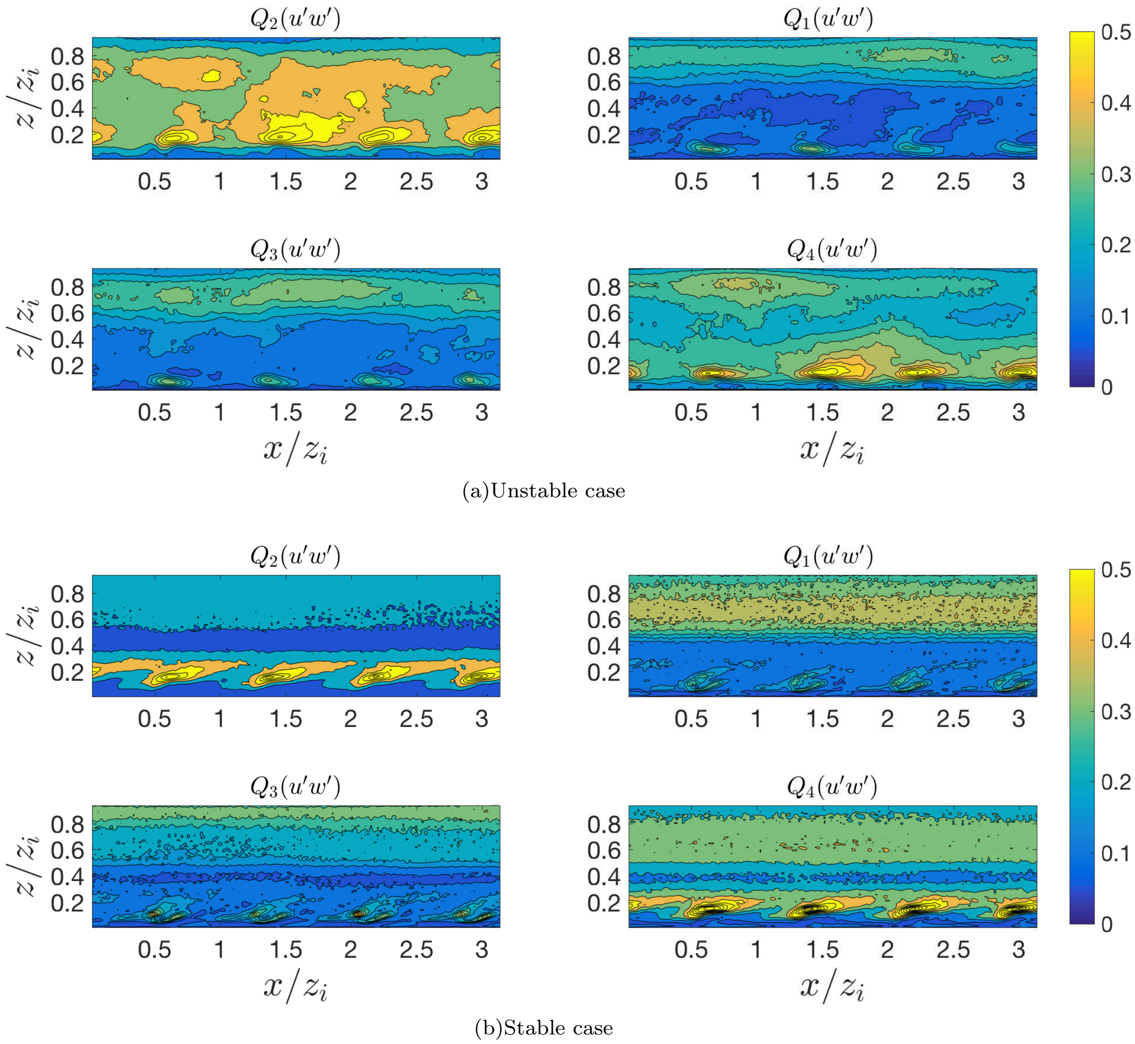

FIG. 11. Quadrant analysis with respect to momentum transport $\langle u'w' \rangle$. The quadrants are normalized via $\sqrt{u'^2 w'^2}$.

from the impact of the stagnation and separation points.

Figure 13 shows the quadrants of the scalar flux based on the wall-normal velocity component and pressure $\langle w'p' \rangle$ for the considered plane. The unstable scenario is marked with a significant sweep and ejection. This trend is related to the vertical transport of mean kinetic energy. The contentious layer is formed in the wake region, where it extends along the streamwise direction of the domain. These observations specifically distinguish the directionality of the fluctuations that change the flow structure and highlight the redistribution of the turbulent kinetic energy and validity of the return-to-isotropy method. Also, the distributions are quite different in the region of the turbine, where rotation is important, and are then minimized above the perturbation region. In addition, a difference in the flow structure implies that the variation occurs concurrently with vertical mean kinetic transport in the wake region. The stable case presented in Figure 13(b) shows that the four quadrants share approximately the same contribution for the vertical scalar flux. The maximum events happen in the wake region, where they are marked from near the surface to above the top tip.

The linkage between turbulent structures and scalar transport based on the streamwise velocity component and temperature $\langle u'\theta' \rangle$ is presented in Figure 14. The unstable case shows that the unperturbed layers are marked with maximum positive scalar transport, shown by quadrants 1 and 3. In contrast to the lower layer of the flow that is marked with negative transport. Sweep events exceed other types in this region. In the stable case, the positive scalar transport is dominant and the negative transport is relatively small, which is consistent with the fact that temperature generally increases with height in stable conditions. The mean scalar sweep and ejection fractions are independent on height and they are constant from the hub height to 800 m above the surface.

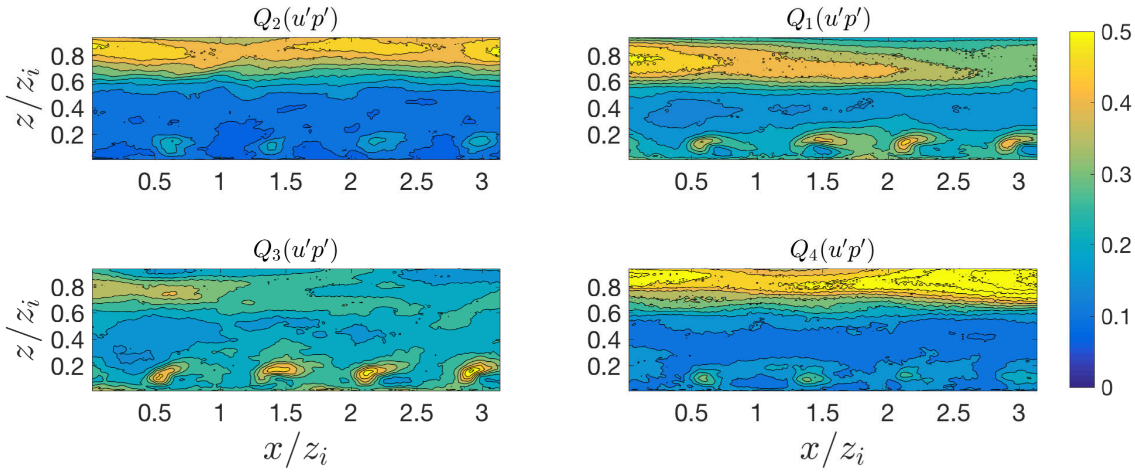

(a)Unstable case

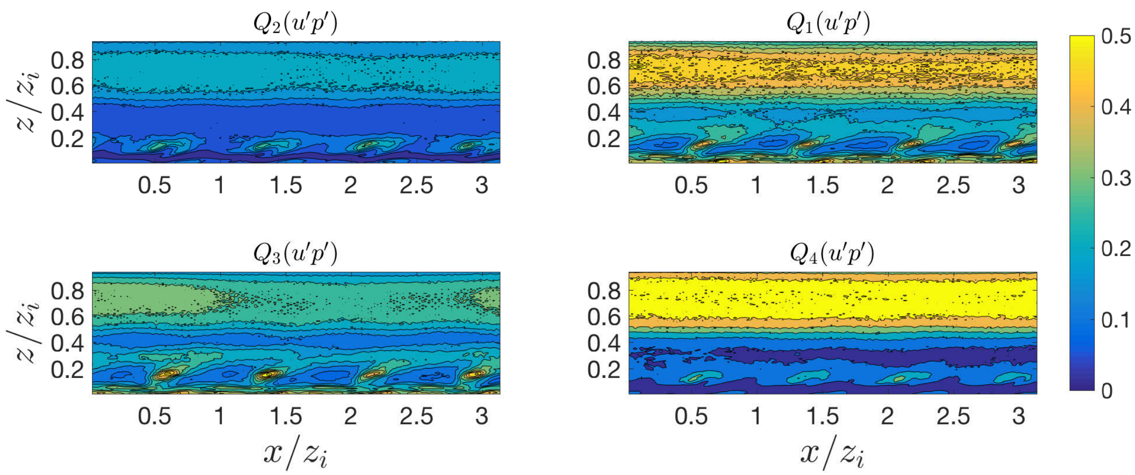

(b)Stable case

FIG. 12. Quadrant analysis with respect to scalar transport $\langle u'p' \rangle$. The quadrants are normalized via $\sqrt{u'^2 p'^2}$.

Figure 15 presents the scalar flux based on the wall-normal velocity component and temperature $\langle w'\theta' \rangle$. By considering the flow layer, the events can be classified into two regions including the outer region, and the inner region that includes the wake and near-wall regions. The outer region is characterized by a dominantly negative vertical flux. The wake region and below show a maximum positive scalar flux in quadrant 1. For the stable case, the four quadrants are comparable, where they display maximum flux at the wake region and above. Above the shear layer the flux becomes independent of height. The thermal stability plays a role in the dissimilarity between the momentum and scalar flux, where the buoyancy modifies the turbulent coherent structures [39]. These structures are responsible for a large fraction of the transport mechanism.

VI. VELOCITY-INTERMITTENCY QUADRANT ANALYSIS

The variation in the turbulent kinetic energy processes through the wind farm, wake-wake interaction, and wake-ABL interactions increases the complexity of this flow. In the wind farm, intermittency represents the irregular alternation of phases of chaotic dynamics that generate variable dynamic loading and increases the fatigue on the blades as well as the gearboxes of the wind turbines [89–93]. Different models are used to analyze intermittency on the wind farm [94–96]. Intermittency in the power increments is higher than the velocity increments due to the large amplitude fluctuations with frequent wind gusts [97]. The flow in the wind farm is characterized by highly intermittent processes over a wide range of scales [98]. Here, the multifractal approach is used to quantify the intermittency as

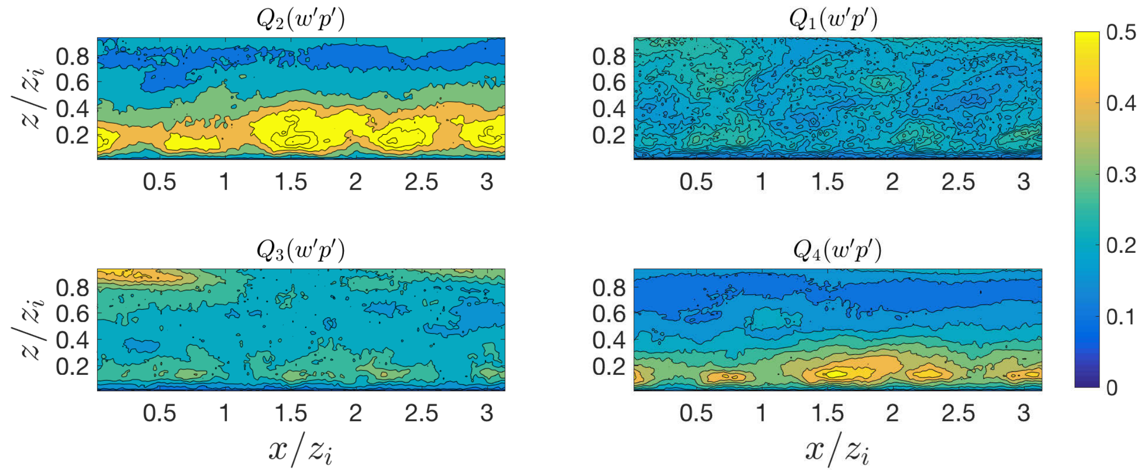

(a)Unstable case

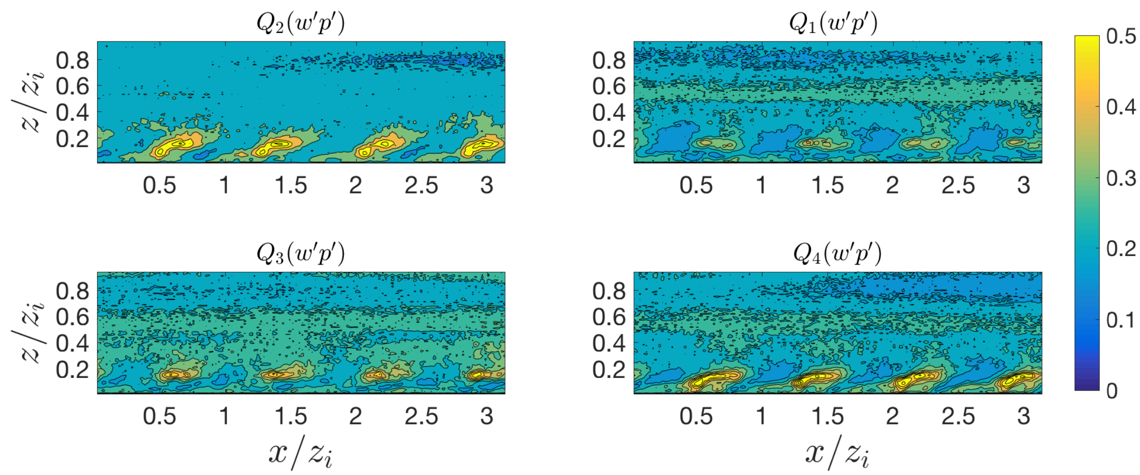

(b)Stable case

FIG. 13. Quadrant analysis with respect to scalar transport $\langle w'p' \rangle$. The quadrants are normalized by $\sqrt{w'^2 p'^2}$.

a function on the stability condition. The intermittency is highlighted by the pointwise Hölder exponent that is connected to the structure function using the Frisch-Parisi conjecture [99, 100]:

$$F(\alpha) = \min_n(\alpha'(t)n - \Psi_n + 1), \tag{17}$$

where $\alpha'(t)$ is the pointwise Hölder exponents for streamwise velocity component u' and Ψ_n is the structure function scaling exponent of the n^{th} moment. The pointwise Hölder exponent can be defined via the differentiability of a signal relative to polynomial expansions as [100–102].

$$\mathbb{P}(t) = \sum_{i=0}^{l-1} \frac{u'^i(t_0)}{i!}(t - t_0)^i, \tag{18}$$

where u' is the velocity in a vicinity, δ, at time t_0, and l is the number of times that velocity time series is differentiable in $t_0 \pm \delta$. The differentiation in a time series is determined though the finite difference between a location of interest and its vicinity. By definition, u': $\mathbb{R}^1 \to \mathbb{R}$ and $t_0 \in \mathbb{R}$; $u \in C^s(t_0)$ if

$$|u'(t) - \mathbb{P}(t)| \leq C\,|t - t_0|^{\Gamma}, \tag{19}$$

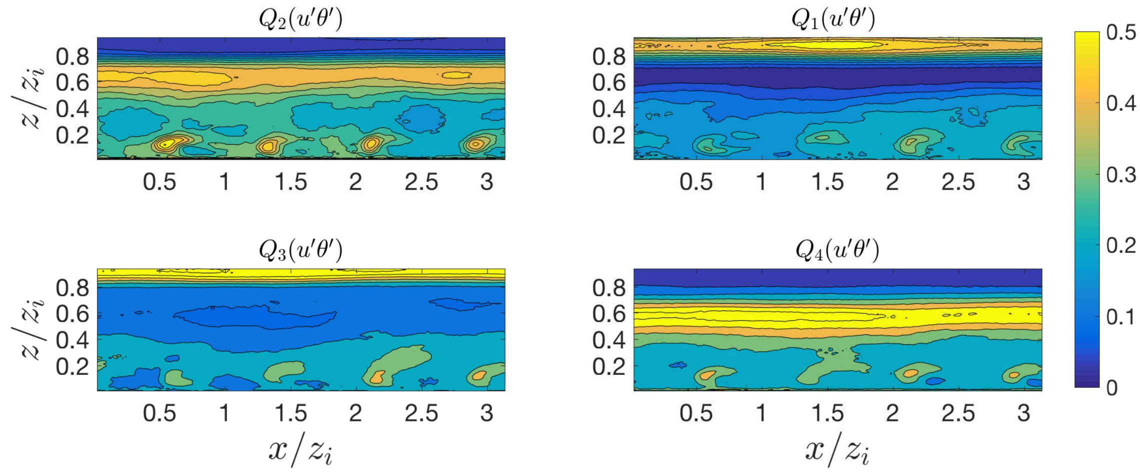

(a)Unstable case

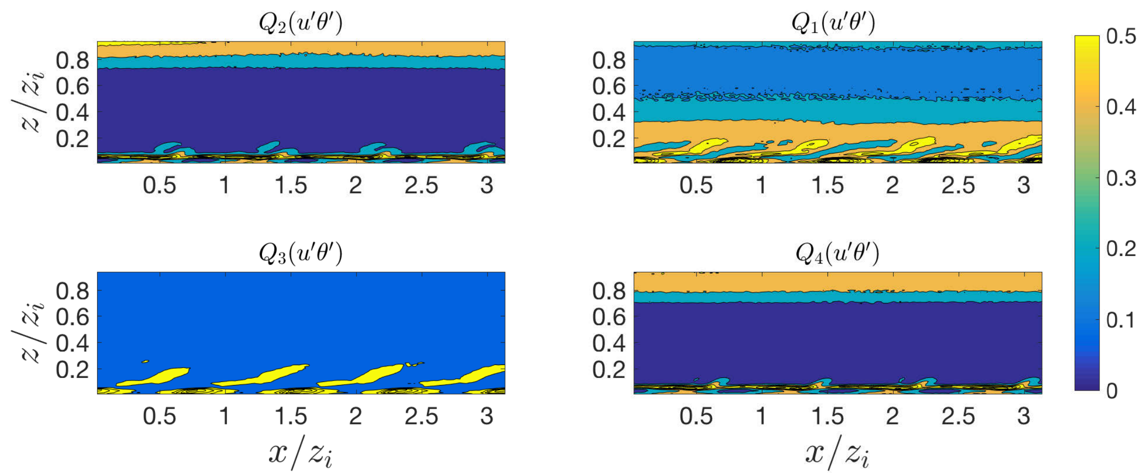

(b)Stable case

FIG. 14. Quadrant analysis with respect to scalar transport $\langle u'\theta' \rangle$. The quadrants are normalized by $\sqrt{u'^2\theta'^2}$.

TABLE II. Four quadrants based on the velocity and pointwise Hölder exponent signs.

Quadrant	sign(u')	sign(α')
Q_1	$+$	$+$
Q_2	$-$	$+$
Q_3	$-$	$-$
Q_4	$+$	$-$

where C is a constant. The pointwise Hölder exponent α' is given by the supremum of Γ that fulfills equation (19) [101, 103]. By analyzing the oscillations of a signal around each point, the Hölder exponent is determined from a log-log regression of these oscillations, $O_{t_0 \pm \delta}$, [104–106]. To quantify the intermittency structure and the velocity-intermittency correlation, the traditional quadrant analysis is modified by replacing the fluctuating vertical velocity component by the fluctuating pointwise Hölder exponent [106–108]. The data are classified based on the sign of the fluctuating terms as shown in Table II. The classification is achieved by having fluctuations greater or less than the zero centered mean ($u' > 0$ and $u' < 0$, respectively) as well as considering a low or high intermittency of the velocity signal ($\alpha' > 0$ and $\alpha' < 0$, respectively) [100, 108–110].

Figure 16 presents the four quadrants of velocity-intermittency for considered cases. The opposite algebraic signs of the second and fourth quadrants are shown for a consistent range with Q_1 and Q_3. For the unstable thermal

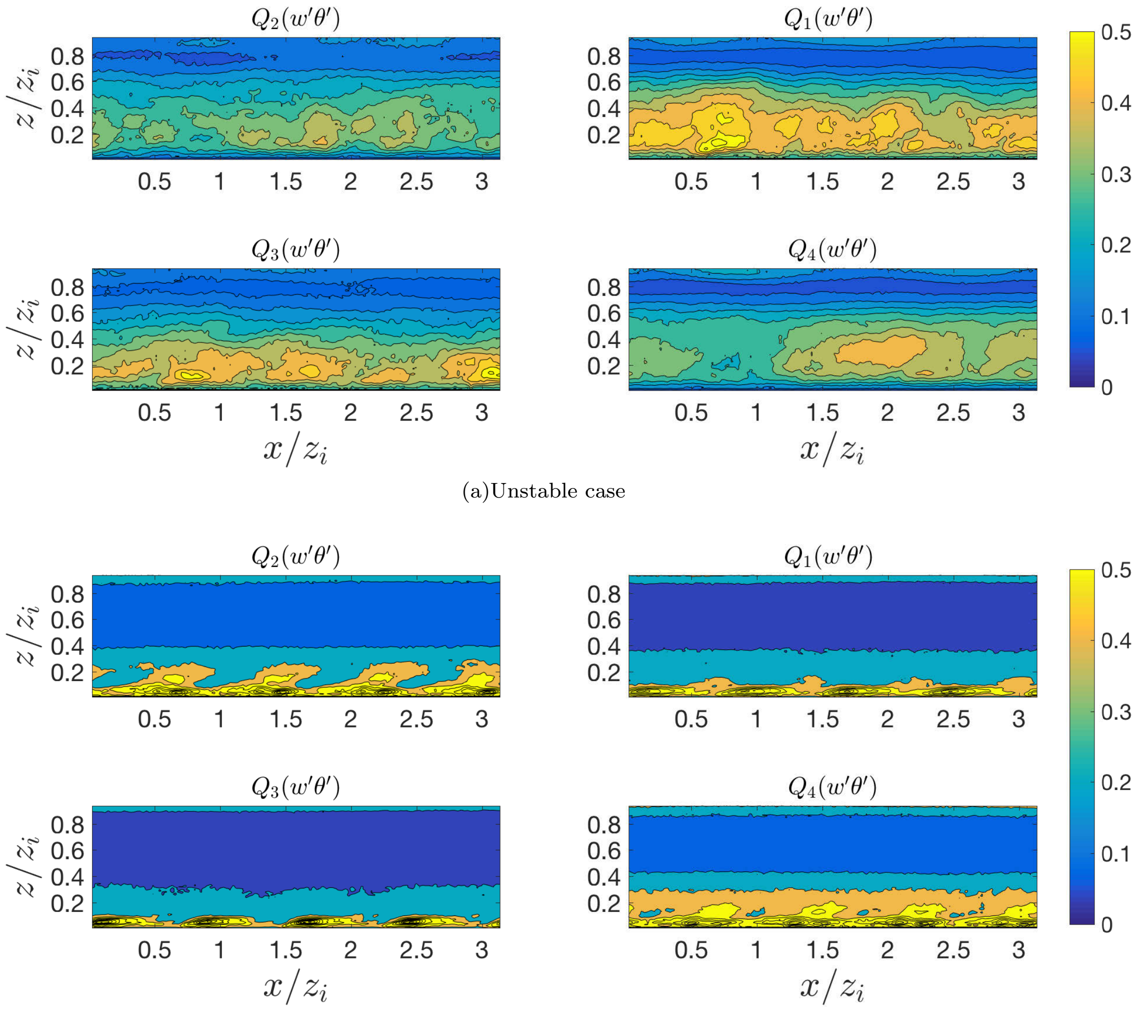

(a)Unstable case

(b)Stable case

FIG. 15. Quadrant analysis with respect to scalar transport $\langle w'\theta' \rangle$. The quadrants are normalized by $\sqrt{w'^2\theta'^2}$.

condition, the first and third quadrants are dominant and contribute most to the total coupling between the velocity and intermittency. From this figure, one can observe that the correlation between the velocity and intermittency are quite dependent on the streamwise and wall-normal locations. The maximum correlation between the velocity and intermittency is observed at the higher layers of the flow and the wake regions, where the low-speed momentum region is marked with higher intermittency. The locations above the rotors are influenced by the shear layer and show a positive correlation (Q_3) due to the entrainment contributions from the unperturbed region. The degree of the correlation is sharply increased at the higher layers of the domain. The stable case shows the dominance of the third quadrant in the wake region and the fourth quadrant in the higher layers of the domain. In this case, the footprint of the intermittency extends to cover the distances between the rotors, and extends to the shear layer above the rotor. The wake-wake interactions are marked with dominance of the first and third quadrants. The extreme velocity-intermittency states preferentially exhibit a negative correlation in the LLJ region. The intermittent wake drives the intermittent power production by a wind farm seen in the diurnal cycle.

VII. CONCLUSION

Turbulent kinetic energy transfer processes in wind turbine wakes are among the key remaining challenges for turbulence closure models of wind turbine array boundary layer flow. Details of the TKE process in the wind farms are illustrated here using two different thermal stability conditions (stable and unstable cases) simulated via large

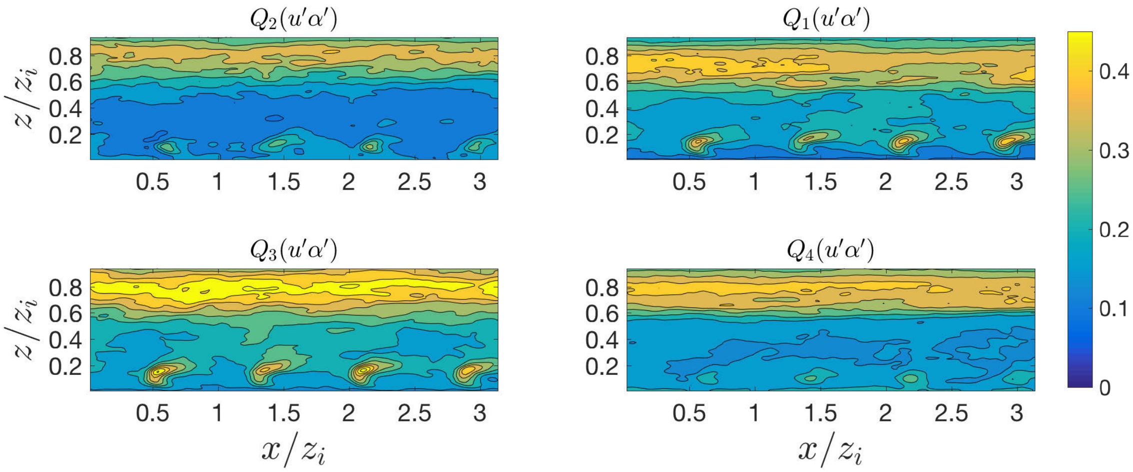

(a)Unstable case

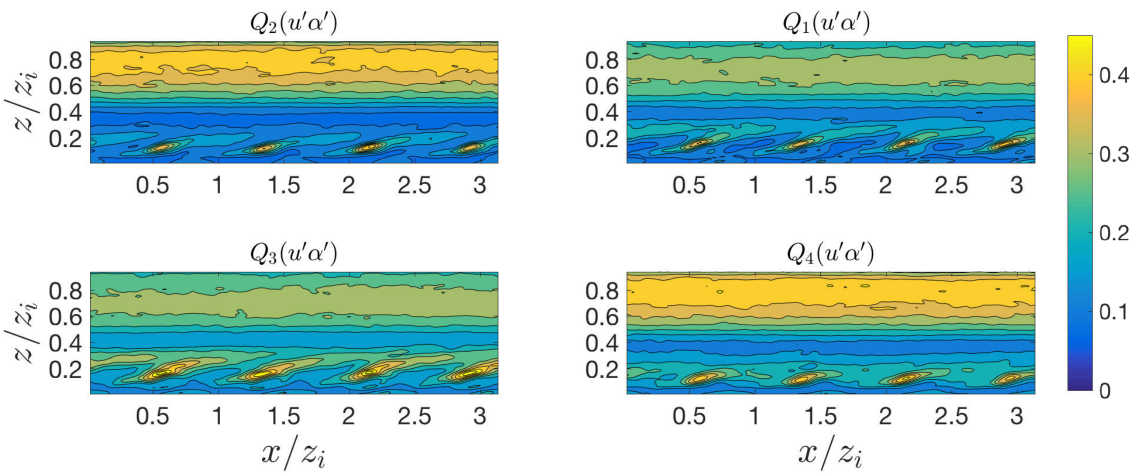

(b)Stable case

FIG. 16. Quadrant analysis with respect to velocity and Hölder exponent $\langle u'\alpha' \rangle$. The quadrants are normalized via $\sqrt{u'^2\alpha'^2}$.

eddy simulations. The effect of thermal stratification on the turbulent kinetic energy budget of the flow is analyzed showing that the order of magnitude of certain terms in the TKE budget are higher for the unstable case than for the stable case. In the wake region, different mechanisms dominate, such as the production, advection, pressure diffusion, and enhanced dissipation by rotor drag. These mechanisms are less important above the shear layer, especially for the stable case. The detailed analysis of the TKE shows that shear production and transport reach a peak at turbine-top level as a result of higher wind shear and turbulent fluxes in that region. The turbulent transport term is responsible for redistribution of the turbulent kinetic energy from the region above the wind plant downward. Pressure diffusion redistributes the TKE generated in the streamwise direction into the other normal components of the Reynolds stress tensor. Triple correlations of the velocity components are a part of the process that energizes the wake region, although they are attenuated by buoyancy force. Marginal correlations are observed in the stable case and the covariance of velocity-temperature and velocity-pressure are enhanced in the lower and middle parts of the unstable case. Reduced form of the TKE budget highlights the most important terms that have significant contribution in the energy balance.

Conditional sampling is used in this study to identify the eddy motion for momentum and scalar transport. The momentum ejection and sweep frequencies are comparable and dominant. The scalar sweep time fraction is independent on height. Within the wake region, the drag of the wind rotors on the flow is extended in the vertical rather than being confined to the ground plane and streamwise direction. Outside of the swept area of the rotors, turbulence decays near the top of the ABL, where there is a balance between the transport, buoyancy, dissipation, and production. Sweep type coherent structures dominate close to and within the wake, whereas ejections gain importance above rotor area. In the stable case, the flow shows distinct layers of turbulence created by mechanical shear. The coherent exchange in the transporting scalar flux exceeds that for momentum.

With this approach one can define the region of the wind farm participating in the exchange of energy with the ABL under different thermal stability conditions. In the unstable case, no balance between sweep and ejection fluxes is observed in the momentum flux because buoyancy performs upward fluxes and intense ejections surrounded by weaker longer sweeps, especially in the wake region. A complex pattern of sweep events can be seen in the top tip region as a result of the vortex shedding. With increasing thermal stability, the sweep and ejection events balance due to the contribution of the buoyancy term. Transport efficiency based on quadrant analysis is examined showing that the pressure-based transport increases when the buoyancy term increases, and that momentum transport decreases sharply.

Quadrant analysis is extended to investigate the intermittency based on the pointwise Hölder exponents. The streamwise velocity and intermittency are correlated quite differently in the wake and locations above the wind plant. The positive correlations are dominant in the wake and higher layer of the domain for unstable case. In contrast, the stable case is marked with the negative correlation. Turbulent exchange processes require further investigations with different stability conditions. A matching asymptotic approach is required to make a link between the local thermal and convective structures.

The current study highlights the impact of specific cases of thermal stratification on the local turbulent kinetic energy budget on a characteristics wind farm. The implications of other stability levels can affect on the energy balance among the terms of the budget, especially in the surface layer, where the mechanical production and the thermal production are in balance. As highlighted in Abkar and Porté-Agel [14] the thermal stability impacts the location of the maximum TKE downstream the rotors, and the the spatial distribution of the turbulence production, dissipation and transport terms. Therefore, increasing or decreasing the level of the stability will make the turbulence are dominant with thermal shear or mechanical shear, respectively.

VIII. ACKNOWLEDGEMENTS

The authors would like to recognize the computational support provided by the Center for High Performance Computing (CHPC) at University of Utah. This work was authored in part by Alliance for Sustainable Energy, LLC, the manager and operator of the National Renewable Energy Laboratory for the U.S. Department of Energy (DOE) under Contract No. DE-AC36-08GO28308. Funding provided by the U.S. Department of Energy Office of Energy Efficiency and Wind Energy Technologies Office. The views expressed in the article do not necessarily represent the views of the DOE or the U.S. government. The U.S. Government retains and the publisher, by accepting the article for publication, acknowledges that the U.S. government retains a nonexclusive, paid-up, irrevocable, worldwide license to publish or reproduce the published form of this work, or allow others to do so, for U.S. government purposes.

[1] R. Stull, An Introduction to Boundary Layer Meteorology, Atmospheric Science Library, Springer, 1988.
[2] N. Ali, N. Hamilton, G. Cortina, M. Calaf, R. B. Cal, Anisotropy stress invariants of thermally stratified wind turbine array boundary layers using large eddy simulations, Journal of Renewable and Sustainable Energy 10 (1) (2018) 013301.
[3] N. Ali, N. Hamilton, D. DeLucia, R. B. Cal, Assessing spacing impact on coherent features in a wind turbine array boundary layer, Wind Energy Science 3 (1) (2018) 43–56.
[4] N. Ali, A. Aseyev, M. Melius, M. Tutkun, R. B. Cal, Evaluation of Higher Order Moments and Isotropy in the Wake of a Wind Turbine Array, in: Whither Turbulence and Big Data in the 21st Century?, Springer., 273–292, 2017.
[5] R. B. Cal, J. Lebrón, L. Castillo, H. S. Kang, C. Meneveau, Experimental study of the horizontally averaged flow structure in a model wind-turbine array boundary layer, Journal of Renewable and Sustainable Energy 2 (1) (2010) 013106.
[6] M. Calaf, C. Meneveau, J. Meyers, Large eddy simulation study of fully developed wind-turbine array boundary layers, Physics of fluids 22 (1) (2010) 015110.
[7] K. Viestenz, R. B. Cal, Streamwise evolution of statistical events in a model wind-turbine array, Boundary-layer meteorology 158 (2) (2016) 209–227.
[8] G. Cortina, R. B. Cal, M. Calaf, Distribution of mean kinetic energy around an isolated wind turbine and a characteristic wind turbine of a very large wind farm, Physical Review Fluids 074402 (2016) 1–18.
[9] L. Chamorro, F. Porté-Agel, Effects of thermal stability and incoming boundary-layer flow characteristics on wind-turbine wakes: a wind-tunnel study, Boundary-Layer Meteorology 136 (2010) 515–533.
[10] W. Zhang, C. D. Markfort, F. Porté-Agel, Wind-turbine wakes in a convective boundary layer: a wind-tunnel study, Boundary-layer meteorology 146 (2) (2013) 161–179.
[11] R. J. Barthelmie, L. E. Jensen, Evaluation of wind farm efficiency and wind turbine wakes at the Nysted offshore wind farm, Wind Energy 13 (2010) 573–586.

[12] S. Xie, C. L. Archer, A numerical study of wind-turbine wakes for three atmospheric stability conditions, Boundary-Layer Meteorology 165 (1) (2017) 87–112.
[13] N. S. Ghaisas, C. L. Archer, S. Xie, S.and Wu, E. Maguire, Evaluation of layout and atmospheric stability effects in wind farms using large-eddy simulation, Wind Energy 20 (7) (2017) 1227–1240.
[14] M. Abkar, F. Porté-Agel, Influence of atmospheric stability on wind-turbine wakes: A large-eddy simulation study, Physics of Fluids 27 (3) (2015) 035104.
[15] M. Abkar, F. Porté-Agel, Mean and turbulent kinetic energy budgets inside and above very large wind farms under conventionally-neutral condition, Renewable Energy. 70 (2014) 142–152.
[16] L. P. Chamorro, M. Guala, R. E. A. Arndt, F. Sotiropoulos, On the evolution of turbulent scales in the wake of a wind turbine model, Journal of Turbulence (13) (2012) N27.
[17] J. Wilson, A second-order closure model for flow through vegetation, Boundary-Layer Meteorology 42 (4) (1988) 371–392.
[18] M. Y. Leclerc, R. H. Shaw, G. D. Hartog, H. H. Neumann, The influence of atmospheric stability on the budgets of the Reynolds stress and turbulent kinetic energy within and above a deciduous forest, Journal of Applied Meteorology 29 (9) (1990) 916–933.
[19] A. Morse, B. Gardiner, B. Marshall, Mechanisms controlling turbulence development across a forest edge, Boundary-Layer Meteorology 103 (2) (2002) 227–251.
[20] C.-H. Moeng, J. C. Wyngaard, An analysis of closures for pressure-scalar covariances in the convective boundary layer, Journal of the Atmospheric Sciences 43 (21) (1986) 2499–2513.
[21] A. Andrén, C.-H. Moeng, Single-point closures in a neutrally stratified boundary layer, Journal of the Atmospheric Sciences 50 (20) (1993) 3366–3379.
[22] D. V. Mironov, Pressure-potential-temperature covariance in convection with rotation, Quarterly Journal of the Royal Meteorological Society 127 (571) (2001) 89–110.
[23] N. L. Miles, J. C. Wyngaard, M. J. Otte, Turbulent pressure statistics in the atmospheric boundary layer from large-eddy simulation, Boundary-layer meteorology 113 (2) (2004) 161–185.
[24] D. V. Mironov, Turbulence in the lower troposphere: Second-order closure and mass–flux modelling frameworks, in: Interdisciplinary Aspects of Turbulence, Springer, 1–61, 2008.
[25] J. Rotta, Statistische theorie nichthomogener turbulenz, Zeitschrift für Physik 129 (6) (1951) 547–572.
[26] B. Launder, G. J. Reece, W. Rodi, Progress in the development of a Reynolds-stress turbulence closure, Journal of Fluid Mechanics 68 (3) (1975) 537–566.
[27] J. L. Lumley, Computational modeling of turbulent flows, in: Advances in applied mechanics, vol. 18, Elsevier, 123–176, 1979.
[28] J. Ristorcelli, J. L. Lumley, R. Abid, A rapid-pressure covariance representation consistent with the Taylor-Proudman theorem materially frame indifferent in the two-dimensional limit, Journal of Fluid Mechanics 292 (1995) 111–152.
[29] T. Craft, N. Ince, B. Launder, Recent developments in second-moment closure for buoyancy-affected flows, Dynamics of atmospheres and oceans 23 (1-4) (1996) 99–114.
[30] J. Wilczak, Large-scale eddies in the unstably stratified atmospheric surface layer. Part I: Velocity and temperature structure, Journal of the atmospheric sciences 41 (24) (1984) 3537–3550.
[31] J. M. Wilczak, A. J. Bedard Jr, A new turbulence microbarometer and its evaluation using the budget of horizontal heat flux, Journal of Atmospheric and Oceanic Technology 21 (8) (2004) 1170–1181.
[32] Y. Naka, M. Stanislas, J. Foucaut, S. Coudert, J. Laval, S. Obi, Space–time pressure–velocity correlations in a turbulent boundary layer, Journal of Fluid Mechanics 771 (2015) 624–675.
[33] M. Raupach, R. Shaw, Averaging procedures for flow within vegetation canopies, Boundary-Layer Meteorology 22 (1) (1982) 79–90.
[34] S. Shah, E. Bou-Zeid, Very-large-scale motions in the atmospheric boundary layer educed by snapshot proper orthogonal decomposition, Boundary-Layer Meteorology 153 (3) (2014) 355–387.
[35] C. VerHulst, C. Meneveau, Large eddy simulation study of the kinetic energy entrainment by energetic turbulent flow structures in large wind farms, Physics of Fluids 26 (2), ISSN 10897666.
[36] N. Hamilton, M. Tutkun, R. B. Cal, Wind turbine boundary layer arrays for Cartesian and staggered configurations: Part II, low-dimensional representations via the proper orthogonal decomposition, Wind Energy 18 (2) (2015) 297–315.
[37] H. F. Kadum, D. Knowles, C. R. B., Quantification of preferential contribution of Reynolds shear stresses and flux of mean kinetic energy via conditional sampling in a wind turbine array, Journal of Fluids Engineering 141 (2) (2019) 021201.
[38] I. Esau, The Coriolis effect on coherent structures in planetary boundary layers, Journal of Turbulence 5248 (03) (2003) 1–20, ISSN 14685248.
[39] N. Ali, G. Cortina, N. Hamilton, M. Calaf, R. B. Cal, Turbulence characteristics of a thermally stratified wind turbine array boundary layer via proper orthogonal decomposition, Journal of Fluid Mechanics 828 (2017) 175–195.
[40] S. S. Lu, W. W. Willmarth, Measurements of the structure of the Reynolds stress in a turbulent boundary layer, Journal of Fluid Mechanics 60 (3) (1973) 481–511.
[41] H. Nakagawa, I. Nezu, Prediction of the contributions to the Reynolds stress from bursting events in open-channel flows, Journal of Fluid Mechanics 80 (1) (1977) 99–128.
[42] R. A. Antonia, Conditional sampling in turbulence measurement, Annual review of fluid mechanics 13 (1) (1981) 131–156.
[43] D. G. Bogard, W. G. Tiederman, Burst detection with single-point velocity measurements, Journal of Fluid Mechanics 162 (1986) 389–413.
[44] G. Katul, G. Kuhn, J. Schieldge, C.-I. Hsieh, The ejection-sweep character of scalar fluxes in the unstable surface layer, Boundary-Layer Meteorology 83 (1) (1997) 1–26.

[45] C. Barthlott, P. Drobinski, C. Fesquet, T. Dubos, C. Pietras, Long-term study of coherent structures in the atmospheric surface layer, Boundary-Layer Meteorology 125 (1) (2007) 1–24.
[46] Z. Mo, C. Liu, A wind tunnel study of ventilation mechanism over hypothetical urban roughness: The role of intermittent motion scales, Building and Environment 135 (2018) 94–103.
[47] D. Guan, P. Agarwal, Y. Chiew, Quadrant analysis of turbulence in a rectangular cavity with large aspect ratios, Journal of Hydraulic Engineering 144 (7) (2018) 04018035.
[48] M. Qi, J. Li, Q. Chen, Q. Zhang, Roughness effects on near-wall turbulence modelling for open-channel flows, Journal of Hydraulic Research (2018) 1–14.
[49] V. Roussinova, A. Shinneeb, R. Balachandar, Investigation of fluid structures in a smooth open-channel flow using proper orthogonal decomposition, Journal of Hydraulic Engineering 136 (3) (2009) 143–154.
[50] B. Viggiano, T. Dib, N. Ali, L. G. Mastin, R. B. Cal, S. A. Solovitz, Turbulence, entrainment and low-order description of a transitional variable-density jet, Journal of Fluid Mechanics 836 (2018) 1009–1049.
[51] Y. Wu, K. T. Christensen, Outer-layer similarity in the presence of a practical rough-wall topography, Physics of Fluids 19 (8) (2007) 085108.
[52] R. J. Volino, M. P. Schultz, C. M. Pratt, Conditional sampling in a transitional boundary layer under high free-stream turbulence conditions, in: ASME Turbo Expo 2001: Power for Land, Sea, and Air, American Society of Mechanical Engineers, V003T01A066–V003T01A066, 2001.
[53] K. P. Nolan, T. A. Zaki, Conditional sampling of transitional boundary layers in pressure gradients, Journal of Fluid Mechanics 728 (2013) 306–339.
[54] N. O. Aksamit, J. W. Pomeroy, The effect of coherent structures in the atmospheric surface layer on blowing-snow transport, Boundary-Layer Meteorology 167 (2) (2018) 211–233.
[55] M. P. Buckley, F. Veron, The turbulent airflow over wind generated surface waves, European Journal of Mechanics-B/Fluids .
[56] W. Zhu, R. Van Hout, J. Katz, PIV measurements in the atmospheric boundary layer within and above a mature corn canopy. Part II: Quadrant-hole analysis, Journal of the Atmospheric Sciences 64 (8) (2007) 2825–2838.
[57] S. Longo, M. A. Losada, Turbulent structure of air flow over wind-induced gravity waves, Experiments in fluids 53 (2) (2012) 369–390.
[58] D. Pokrajac, L. J. Campbell, V. Nikora, C. Manes, I. McEwan, Quadrant analysis of persistent spatial velocity perturbations over square-bar roughness, Experiments in Fluids 42 (3) (2007) 413–423.
[59] C. Thomas, T. Foken, Flux contribution of coherent structures and its implications for the exchange of energy and matter in a tall spruce canopy, Boundary-Layer Meteorology 123 (2) (2007) 317–337.
[60] J. J. Finnigan, Turbulent transport in flexible plant canopies, in: The Forest-Atmosphere Interaction, Springer, 443–480, 1985.
[61] P. A. Coppin, M. R. Raupach, B. J. Legg, Experiments on scalar dispersion within a model plant canopy part II: An elevated plane source, Boundary-Layer Meteorology 35 (1-2) (1986) 167–191.
[62] N. Hamilton, H. Suk Kang, C. Meneveau, R. B. Cal, Statistical analysis of kinetic energy entrainment in a model wind turbine array boundary layer, Journal of Renewable and Sustainable Energy 4 (6) (2012) 063105.
[63] E. Bou-Zeid, C. Meneveau, M. B. Parlange, A scale-dependent Lagrangian dynamic model for large eddy simulation of complex turbulent flows, Physics of Fluids. 17 (2005) 1–18.
[64] M. Calaf, M. B. Parlange, C. Meneveau, Large eddy simulation study of scalar transport in fully developed wind-turbine array boundary layers, Physics of Fluids. 23 (2011) 126603.
[65] V. Sharma, M. Calaf, M. Lehning, M. Parlange, Time-adaptive wind turbine model for an LES framework, Wind Energy 19 (5) (2016) 939–952.
[66] G. Cortina, V. Sharma, M. Calaf, Investigation of the incoming wind vector for improved wind turbine yaw-adjustment under different atmospheric and wind farm conditions, Renewable Energy 101 (2017) 376–386.
[67] G. Cortina, M. Calaf, Turbulence upstream of wind turbines: A large-eddy simulation approach to investigate the use of wind lidars, Renewable Energy 105 (2017) 354–365, ISSN 0960-1481.
[68] C.-H. Moeng, A large-eddy-simulation model for the study of planetary boundary-layer Turbulence, Journal of the Atmospheric Sciences 41 (13) (1984) 2052–2062.
[69] J. D. Albertson, M. B. Parlange, Natural integration of scalar fluxes from complex terrain, Advances in Water Resources 23 (3) (1999) 239–252.
[70] C. Canuto, M. Hussainii, A. Quarteroni, Spectral methods in fluid dynamics, Springer-Verlag, Berlin, 1988.
[71] A. S. Monin, A. M. Obukhov, Basic laws of turbulent mixing in the surface layer of the atmosphere, Tr. Akad. Nauk SSSR Geofiz. Inst. English translation by John Miller, 1959. 24 (151) (1954) 163–187.
[72] M. B. Parlange, W. Brustaert, Regional shear stress of broken forest from radiosonde wind profiles in the unstable surface layer, Boundary-Layer Meteorology 64(4) (1993) 355–368.
[73] W. Brutsaert, M. B. Parlange, The unstable surface layer above forest: Regional evaporation and heat flux, Water Resources Research 28 (12) (1992) 3129–3134.
[74] W. Brutsaert, M. B. Parlange, J. Gash, Neutral humidity profiles in the boundary layer and regional evaporation from sparse pine forest, in: Annales Geophysicae, vol. 7, 623–630, 1989.
[75] W. Brutsaert, Hydrology: An Introduction, Cambridge University Press, 2005.
[76] G. S. Poulos, W. Blumen, D. C. Fritts, J. K. Lundquist, et al., CASES-99: A comprehensive investigation of the stable nocturnal boundary layer, Bulletin of the American Meteorological Society 83 (4) (2002) 555.

[77] V. Sharma, M. Parlange, M. Calaf, Perturbations to the spatial and temporal characteristics of the diurnally-varying atmospheric boundary layer due to an extensive wind farm, Boundary-Layer Meteorology (2016) 1–28.
[78] P. E. Skåre, P.-Å. Krogstad, A turbulent equilibrium boundary layer near separation, Journal of Fluid Mechanics 272 (1994) 319–348.
[79] P.-Å. Krogstad, P. E. Skåre, Influence of a strong adverse pressure gradient on the turbulent structure in a boundary layer, Physics of Fluids 7 (8) (1995) 2014–2024.
[80] M. Marquillie, J.-P. Laval, R. Dolganov, Direct numerical simulation of a separated channel flow with a smooth profile, Journal of Turbulence 9 (2008) N1.
[81] K. Babić, M. W. Rotach, Turbulence kinetic energy budget in the stable boundary layer over a heterogeneous surface, Quarterly Journal of the Royal Meteorological Society .
[82] N. Tobin, H. Zhu, L. P. Chamorro, Spectral behaviour of the turbulence-driven power fluctuations of wind turbines, Journal of Turbulence 16 (9) (2015) 832–846.
[83] H. Liu, Y. Jin, N. Tobin, L. P. Chamorro, Towards uncovering the structure of power fluctuations of wind farms, Physical Review E 96 (6) (2017) 063117.
[84] J. Bossuyt, C. Meneveau, J. Meyers, Wind farm power fluctuations and spatial sampling of turbulent boundary layers, Journal of Fluid Mechanics 823 (2017) 329–344.
[85] S. B. Pope, Simple models of turbulent flows, Physics of Fluids 23 (1) (2011) 011301.
[86] T. P. Meyers, D. D. Baldocchi, The budgets of turbulent kinetic energy and Reynolds stress within and above a deciduous forest, Agricultural and forest meteorology 53 (3) (1991) 207–222.
[87] D. V. Mironov, P. P. Sullivan, Second-moment budgets and mixing intensity in the stably stratified atmospheric boundary layer over thermally heterogeneous surfaces, Journal of the Atmospheric Sciences 73 (1) (2016) 449–464.
[88] M. Y. Zhou, D. H. Lenschow, B. B. Stankov, J. C. Kaimal, J. E. Gaynor, Wave and turbulence structure in a shallow baroclinic convective boundary layer and overlying inversion, Journal of the atmospheric sciences 42 (1) (1985) 47–57.
[89] S. L. Brunton, B. W. Brunton, J. L. Proctor, E. Kaiser, J. N. Kutz, Chaos as an intermittently forced linear system, Nature Communications 8 (1) (2017) 19.
[90] K. Thomsen, H. W. Bindner, T. F. Pedersen, Fatigue loads on a pitch regulated wind turbine operating in a coastal wind turbine array, 1994.
[91] K. Thomsen, P. Sørensen, Fatigue loads for wind turbines operating in wakes, Journal of Wind Engineering and Industrial Aerodynamics 80 (1-2) (1999) 121–136.
[92] H. J. Sutherland, On the fatigue analysis of wind turbines, Tech. Rep., Sandia National Labs., Albuquerque, NM (US); Sandia National Labs., Livermore, CA (US), 1999.
[93] J. F. Manwell, J. G. McGowan, A. L. Rogers, Wind energy explained: theory, design and application, John Wiley & Sons, 2010.
[94] N. Ali, A. S. Aseyev, R. B. Cal, Structure functions, scaling exponents and intermittency in the wake of a wind turbine array, Journal of Renewable and Sustainable Energy 8 (1) (2016) 013304.
[95] B. Viggiano, M. S. Gion, N. Ali, M. Tutkun, R. B. Cal, Inverse structure functions in the canonical wind turbine array boundary layer, Journal of Renewable and Sustainable Energy 8 (5) (2016) 053310.
[96] N. Ali, H. F. Kadum, R. B. Cal, Focused-based multifractal analysis of the wake in a wind turbine array utilizing proper orthogonal decomposition, Journal of Renewable and Sustainable Energy 8 (6) (2016) 063306.
[97] P. Milan, M. Wächter, J. Peinke, Turbulent character of wind energy, Physical Review Letters 110 (13) (2013) 138701.
[98] R. Calif, F. G. Schmitt, Multiscaling and joint multiscaling description of the atmospheric wind speed and the aggregate power output from a wind farm, Nonlinear Processes in Geophysics 21 (2) (2014) 379–392.
[99] G. Parisi, M. Ghil, Turbulence and Predictability in Geophysical Fluid Dynamics and Climate Dynamics: Proceedings of the International School of Physic Enrico Fermi. Course LXXXVIII, Varenna on Lake Como, Villa Monastero, 14-24 June, 1983, North-Holland, 1985.
[100] C. J. Keylock, K. S. Chang, G. S. Constantinescu, Large eddy simulation of the velocity-intermittency structure for flow over a field of symmetric dunes, Journal of Fluid Mechanics 805 (2016) 656–685.
[101] K. M. Kolwankar, J. Lévy-Véhel, A time domain characterization of the fine local regularity of functions, Journal of Fourier Analysis and Applications 8 (4) (2002) 319–334.
[102] S. Jaffard, Multifractal formalism for functions part I: results valid for all functions, SIAM Journal on Mathematical Analysis 28 (4) (1997) 944–970.
[103] S. Seuret, J. Lévy-Véhel, A time domain characterization of 2-microlocal spaces, Journal of Fourier Analysis and Applications 9 (5) (2003) 473–495.
[104] C. Tricot, Curves and fractal dimension, Springer Science & Business Media, 1994.
[105] L. Trujillo, P. Legrand, J. Lévy-Véhel, The estimation of hölderian regularity using genetic programming, in: Proceedings of the 12th Annual Conference on Genetic and Evolutionary Computation, ACM, 861–868, 2010.
[106] C. J. Keylock, Characterizing the structure of nonlinear systems using gradual wavelet reconstruction, Nonlinear Processes in Geophysics 17 (6) (2010) 615.
[107] C. J. Keylock, A criterion for delimiting active periods within turbulent flows, Geophysical Research Letters 35 (11).
[108] C. J. Keylock, K. Nishimura, J. Peinke, A classification scheme for turbulence based on the velocity-intermittency structure with an application to near-wall flow and with implications for bed load transport, Journal of Geophysical Research: Earth Surface 117 (F1).
[109] C. J. Keylock, A. Singh, J. G. Venditti, E. Foufoula-Georgiou, Robust classification for the joint velocity-intermittency structure of turbulent flow over fixed and mobile bedforms, Earth Surface Processes and Landforms 39 (13) (2014)

1717–1728.

[110] C. J. Keylock, B. Ganapathasubramani, J. Monty, N. Hutchins, I. Marusic, The coupling between inner and outer scales in a zero pressure boundary layer evaluated using a Hölder exponent framework, Fluid Dynamics Research 48 (2) (2016) 021405.